








Luminosity predictions for the first three ionization stages of W, Pt, and Au to probe potential sources of emission in kilonova

M. McCann ^{1,★}, L. P. Mulholland ¹, Z. Xiong ², C. A. Ramsbottom ¹, C. P. Ballance ¹, O. Just ^{2,3},
A. Bauswein ^{2,4}, G. Martínez-Pinedo ^{2,5,4}, F. McNeill ¹ and S. A. Sim ¹

¹*Astrophysics Research Centre, School of Mathematics & Physics, Queen's University Belfast, Belfast BT7 1NN, UK*

²*GSI Helmholtzzentrum für Schwerionenforschung, Planckstraße 1, D-64291 Darmstadt, Germany*

³*Astrophysical Big Bang Laboratory, RIKEN Cluster for Pioneering Research, 2-1 Hirosawa, Wako, Saitama 351-0198, Japan*

⁴*Helmholtz Forschungsakademie Hessen für FAIR, GSI Helmholtzzentrum für Schwerionenforschung, Planckstraße 1, D-64291 Darmstadt, Germany*

⁵*Institut für Kernphysik (Theoriezentrum), Fachbereich Physik, Technische Universität Darmstadt, Schlossgartenstraße 2, D-64289 Darmstadt, Germany*

Accepted 2025 February 13. Received 2025 February 7; in original form 2024 November 25

ABSTRACT

A large number of **R**-matrix calculations of electron-impact excitation for heavy elements ($Z > 70$) have been performed in recent years for applications in fusion and astrophysics research. With the expanding interest in heavy ions due to kilonova (KN) events such as AT2017gfo and AT2023vfi, these new data can be utilized for the diagnosis and study of observed KN spectra. In this work, recently computed electron-impact excitation effective collision strengths are used, for the first three ionization stages of tungsten (W, $Z = 74$), platinum (Pt, $Z = 78$), and gold (Au, $Z = 79$), to construct basic collisional radiative models tailored for the late stage nebular phases of KN. Line luminosities are calculated at a range of electron temperatures and densities and the strengths of these lines for a representative ion mass are compared. For the case of W III, these optically thin intensities are additionally used to constrain the mass of this ion in both AT2017gfo and AT2023vfi. Comparing with theoretical predictions of nucleosynthesis yields from neutron star merger simulations, broad agreement with the inferred ion masses of W is found. Furthermore, we highlight the value of W measurements by showing that the abundance of other groups of elements and outflow properties are constrained by exploiting theoretically motivated correlations between the abundance of W and that of lanthanides or third *r*-process peak elements. Based on simple estimates, we also show that constraints on the distribution of tungsten in the ejecta may be accessible through the line shape, which may also yield information on the neutron star merger remnant evolution.

Key words: atomic data – nuclear reactions, nucleosynthesis, abundances – plasmas – scattering – techniques: spectroscopic.

1 INTRODUCTION

Since the observation of the neutron star merger AT2017gfo kilonova (KN) event in 2017 (Pian et al. 2017; Smartt et al. 2017), several theoretical groups have been engaged in the possible identification of spectral features originating from *r*-process heavy elements. To date, there has been confirmation of a P Cygni feature of Sr II at approximately 1 μm (Watson et al. 2019) and another P Cygni feature of Y II at 760 nm (Sneppen & Watson 2023). Collisional data using the **R**-matrix method for the corresponding transitions of these two features have since been calculated by Mulholland et al. (2024a). In addition, a broad emission feature at 2.1 μm has been suggested by Hotokezaka et al. (2023) and Gillanders et al. (2024), originating from a forbidden transition between the fine-structure levels of the ground configuration of Te III. This interpretation has been supported by non-local thermodynamic equilibrium (NLTE) modelling by Hotokezaka et al. (2023) and more recently by Mulholland et al. (2024b) using newly computed atomic data. A similar feature in

AT2023vfi has also been investigated by Gillanders & Smartt (2024), Levan et al. (2024), and Mulholland et al. (2024b).

Other potential sources of the KN emission have been investigated by Hotokezaka et al. (2022) when interpreting the observations of AT2017gfo by the *Spitzer* space telescope (Villar et al. 2018; Kasliwal et al. 2022) in the late nebular phase at 43–74 d post-merger. Strong emission was observed at 4.5 μm and potential sources were listed as either Se III if the first *r*-process peak elements are abundant or W III otherwise. Modelling this 4.5 μm emission line was difficult due to the lack of accurate atomic data (i.e. wavelengths, Einstein A-coefficients, and collisional electron-impact excitation rates) necessary for the NLTE modelling. In the analysis performed by Hotokezaka et al. (2022), calibrated wavelengths were obtained from the National Institute of Standards and Technology (NIST) data base (Kramida et al. 2024) and the Einstein A-coefficients were calculated using a formula derived by Pasternack (1940), Shortley (1940), and Bahcall & Wolf (1968) for M1 dipole transitions assuming that LS coupling is valid. The collisional atomic data were computed using the HULLAC code (Bar-Shalom, Klapisch & Oreg 2001) for transitions among the levels of the ground terms but otherwise a value of unity was assumed for the effective collision strengths. The

* E-mail: michael.mccann@qub.ac.uk

authors themselves conclude that more accurate atomic data would be required to perform a more detailed analysis. The conclusions from this investigation found that the mid-infrared (mid-IR) spectrum of AT2017gfo could match the synthetic spectrum at 4.5 μm and the associated line would originate from Se III if the first r -process peak elements were abundant, but if the ejecta were dominated by elements beyond the first peak then W III would be a more realistic candidate with an associated W II line emerging at 6.05 μm .

There are, however, more recent atomic data now available in the literature for the first three ionization stages of W. In Smyth et al. (2018), Dirac \mathbf{R} -matrix evaluations for the electron-impact excitation of W I are provided, Dunleavy et al. (2022) compute similar quality \mathbf{R} -matrix data for W II, and more recently McCann et al. (2024) for W III. Using calibrated energy levels from NIST, these three publications provide accurate Einstein A-values and effective collision strengths for a wide variety of incident electron temperatures. In this paper, NLTE collisional radiative modelling is performed using these new atomic data sets for W I, W II, and W III, to compute photon luminosity predictions to further investigate the W III identification proposed by Hotokezaka et al. (2022) for the 4.5 μm forbidden line. The observability of the expected 6.05 μm W II feature is also explored, which shows similar luminosities to the 4.5 μm line when ion masses similar to that of W III are incorporated into the model. Additionally, the mass estimates of W III in AT2017gfo from Hotokezaka et al. (2022) are revised using the newly calculated \mathbf{R} -matrix data and a first mass estimate for W III in AT2023vfi is provided. The mass estimates for W III are used to compare with theoretically predicted nucleosynthesis yields; the implications of the W measurements for the production of other heavy elements such as lanthanides, actinides, and third-peak r -process elements can then be investigated. The mass estimate of W is also important to understand its production by the r -process. So far, it has been observed in only a few metal-poor stars (Roederer et al. 2022).

W is just one element located near the third r -process peak. Accurate \mathbf{R} -matrix calculations have also been performed for the first three ionization stages of Pt and Au, see Bromley et al. (2023) and McCann et al. (2022), respectively. For completeness, the photon luminosity calculations are repeated for both Pt and Au.

The outline of the paper is as follows. In Section 2, the general theory of collisional radiative modelling and the calculation of optically thin luminosity emission spectra is reviewed. In Section 3, synthetic spectra at late-time KN relevant conditions are presented. In addition, representative luminosities are presented for the 10 strongest lines of the first 3 ion stages of W, Pt, and Au. Mass estimates of W III in both AT2017gfo and AT2023vfi are made with the parameter space of electron density and temperature explored. Furthermore in Section 4, the implications of the mass measurements based on comparisons with hydrodynamical neutron star merger simulations and nucleosynthesis calculations are discussed. In Section 5, the velocity distribution in the ejecta is investigated and its potential constraints on the observed line widths. Finally in Section 6, the paper is concluded with a summary and outlook.

2 THEORY

For a specific ion, the population of a level i relative to the ground state, N_i , can be determined from the collisional radiative equations (Bates, Kingston & McWhirter 1962; Summers et al. 2006),

$$\frac{dN_i}{dt} = \sum_j \mathbf{C}_{ij} N_j, \quad (1)$$

where the matrix \mathbf{C}_{ij} encompasses the rates of all the considered atomic processes connecting levels i and j . The above formulation includes the rates of all atomic processes in the matrix \mathbf{C}_{ij} . These include electron-impact excitation/de-excitation, spontaneous emission, ionization, and recombination. At present, there are very limited data for the accurate modelling of ionization (photoionization or collisional) or recombination for the high- Z elements. Therefore, the analysis is restricted to electron-impact excitation/de-excitation and emission. These are likely to be the dominant processes for determining atomic level populations at late times. The time-scales of these atomic processes are very fast compared to the expansion evolution of KN ejecta; therefore, the populations of the different levels can be assumed to be in the steady state. This modelling allows for the estimation of the ion masses in the ejecta but not necessarily elemental ones.

The rates of spontaneous emission and electron-impact excitation and de-excitation have been calculated previously for tungsten (W, $Z = 74$), platinum (Pt, $Z = 78$), and gold (Au, $Z = 79$) (Smyth et al. 2018; Gillanders et al. 2021; Dunleavy et al. 2022; McCann et al. 2022, 2024; Bromley et al. 2023). The reader is referred to these respective articles for the specific details of the \mathbf{R} -matrix calculations. Solving equation (1) for the populations allows for estimations of emission in the steady state. The luminosities are calculated in terms of the photon emissivity coefficient (PEC), typically employed by the fusion community (Summers et al. 2006) and defined by

$$\text{PEC}_{j \rightarrow i} = \frac{N_j A_{j \rightarrow i}}{n_e}, \quad (2)$$

where N_j is the upper level population normalized to the ground level, $A_{j \rightarrow i}$ is the Einstein A-coefficient for the transition from j to i , and n_e is the electron density. A PEC is a derived coefficient that is associated with a single spectral line and is often useful for predicting individual spectral line emission. The COLRADPY package (Johnson, Loch & Ennis 2019) is employed to determine the populations and PECs. When calculating a luminosity to infer a specific ion mass, the populations must be re-normalized; this is due to the populations being calculated relative to the ground in equation (1). The populations have been re-normalized to be relative to the total population of the ion by including a factor of $\sum_i N_i$ when calculating the luminosity. The luminosities are therefore defined as

$$L_{j \rightarrow i} = \frac{hc}{\lambda_{j \rightarrow i}} \frac{n_e \text{PEC}_{j \rightarrow i} M_{\text{ion}}}{\sum_i N_i m_{\text{ion}}}, \quad (3)$$

in units of energy per time, where hc/λ is the photon energy, M_{ion} is the mass of the ion in the ejecta, and m_{ion} is the mass of a single ion particle. The ratio of M_{ion} and m_{ion} encodes the number of ions in the ejecta. By imposing some observed specific luminosity, $L_{j \rightarrow i}$, one can then make ion-mass estimates using equation (3). Additionally, model ion spectra can be constructed and directly compared with observation.

3 RESULTS

3.1 Luminosities

The electron density of the KN transient at late epochs is expected to be considerably lower than that of the early times. However, accurate values are difficult to estimate since they will depend on the radioactive heating, composition, and ejecta density structure, which are hard to precisely constrain. Therefore, we will consider a range of electron densities in our analysis, 10^5 – 10^7 cm^{-3} , which are in line with values adopted in previous studies (Hotokezaka et al.

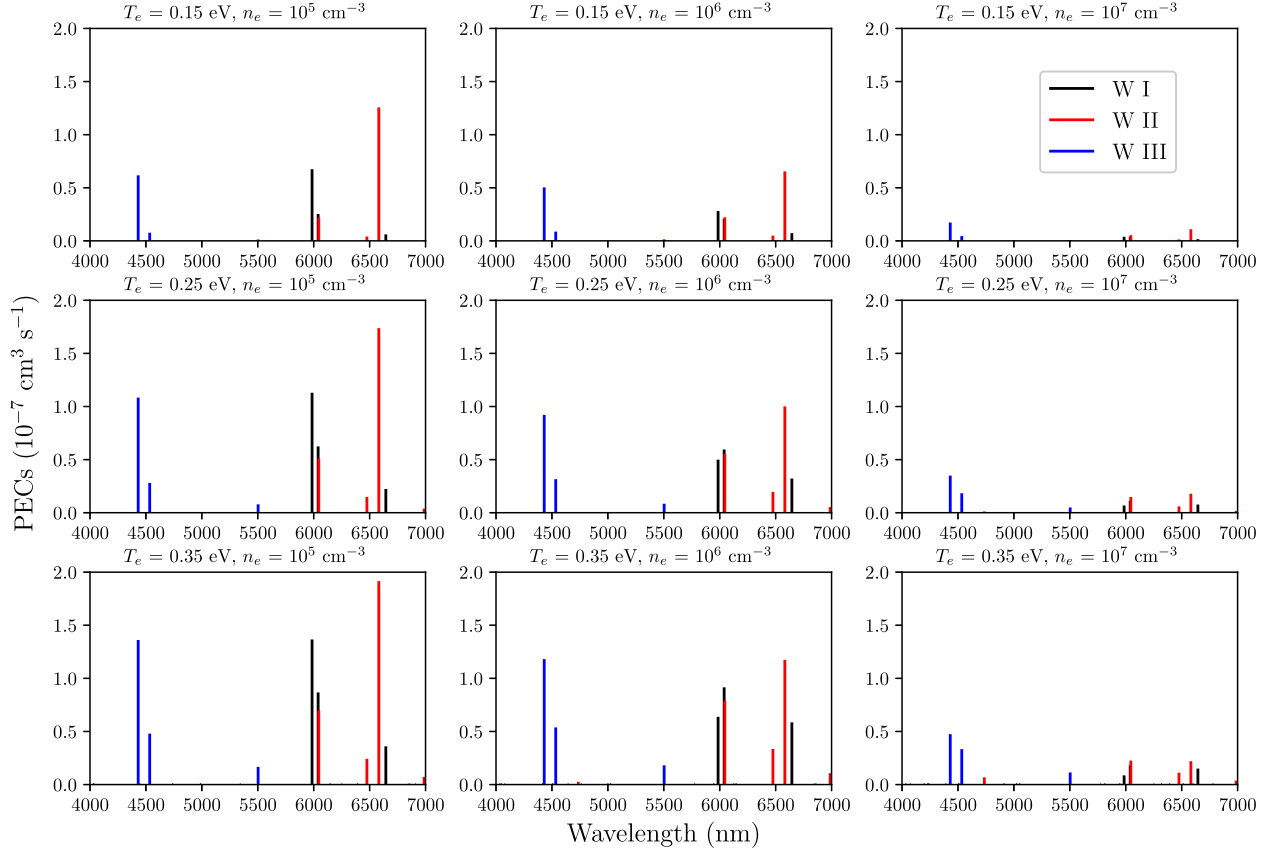


Figure 1. PECs for W I–III for a range of temperatures and densities ($T_e = 0.15, 0.25,$ and 0.35 eV, $n_e = 10^5, 10^6,$ and 10^7 cm $^{-3}$).

2023; Levan et al. 2024), for modelling AT2017gfo and AT2023vfi. Since these densities are below their typical critical densities, M1 transitions among the fine-structure split terms of the ground configuration are expected to give rise to strong emission lines in the IR region of the observed spectrum. All three charge states of W of interest in this publication have fine-structure transitions among their ground state; for W I the ground level has terms $5d^4 6s^2 {}^5D_{0,1,2,3,4}$, for W II $5d^4 6s {}^6D_{1/2,3/2,5/2,7/2,9/2}$, and for W III $5d^4 {}^5D_{0,1,2,3,4}$. W III is of particular interest as it has a strong fine-structure transition coincident with the *Spitzer* space telescope 4.5 μm wavelength range.

In this section, the PECs are investigated, defined in Section 2 (equation 2), for all three ionization stages of W under consideration. In Fig. 1, these PEC coefficients are plotted (in units cm 3 s $^{-1}$) for W I, W II, and W III, as a function of wavelength (nm) from 4000 to 7000 nm spanning the spectrum from the near- to far-IR. Three electron temperatures are considered in the computations, $T_e = 0.15, 0.25,$ and 0.35 eV, and electron densities $n_e = 10^5, 10^6,$ and 10^7 cm $^{-3}$ of relevance to KN modelling. This covers the general temperature and density space used previously in the literature to study specific spectral features (Hotokezaka et al. 2022, 2023; Gillanders et al. 2024; Levan et al. 2024). Clearly evident are three strong W I lines (in black) at 5986.99, 6041.42, and 6646.86 nm, representing the three low-lying forbidden transitions among the ground state terms $5d^4 6s^2 {}^5D_0$ – $5d^4 6s^2 {}^5D_1$, $5d^4 6s^2 {}^5D_1$ – $5d^4 6s^2 {}^5D_3$, and $5d^4 6s^2 {}^5D_3$ – $5d^4 6s^2 {}^5D_4$, respectively. These lines are evident in Fig. 1 at all three temperatures considered and have their highest PEC values at the lower densities of 10^5 and 10^6 cm $^{-3}$. The peak lines of W II (in red) are found at 6047.25, 6477.50, and 6584.02 nm and again represent forbidden transitions among the ground state terms, the $5d^4 6s {}^6D_{3/2}$ –

$5d^4 6s {}^6D_{5/2}$, $5d^4 6s {}^6D_{5/2}$ – $5d^4 6s {}^6D_{7/2}$, and $5d^4 6s {}^6D_{1/2}$ – $5d^4 6s {}^6D_{3/2}$, respectively. The 6041.42 nm line of W I and the 6047.25 nm W II line are very close together in wavelength and could therefore become blended in physical spectra. Finally three strong W III lines (in blue) are predicted at 4432.23, 4535.16, and 5504.75 nm; these correspond to the low-lying forbidden lines $5d^4 {}^5D_0$ – $5d^4 {}^5D_1$, $5d^4 {}^5D_1$ – $5d^4 {}^5D_2$, and $5d^4 {}^5D_2$ – $5d^4 {}^5D_3$, respectively. Hence, two potential W III lines are located around 4.5 μm , where strong emission was detected by the *Spitzer* space telescope (Kasliwal et al. 2022).

To quantify the relative strengths of these 9 forbidden lines, Table 1 gives the calculated luminosities in units ph s $^{-1}$ and erg s $^{-1}$ for the strongest 10 lines of each W ion species. The photon luminosities are computed using equation (3) and adopting a reference mass of 10^{-3} M_\odot , an electron temperature $T_e = 0.15$ eV, and an electron density $n_e = 10^6$ cm $^{-3}$. Clearly, the strongest three lines for each species are those presented in the PEC plot of Fig. 1 and the largest luminosity value of 1.22×10^{38} erg s $^{-1}$ is computed for the W III 4432.23 nm line from the ground state to the first fine-structure split level. It is likely due to large expansion velocities that this will blend with the slightly weaker 4535.16 nm line (\sim factor of 6 for 0.15 eV and 10^6 cm $^{-3}$); therefore, both lines must be considered. This supports the W III prediction made by Hotokezaka et al. (2022) for the 4.5 μm forbidden line. These calculations also support the existence of a strong line at 6.05 μm , the candidates for which could be either W I or W II, due to blending in this wavelength region. This statement is subject to the ion mass of W I or W II being comparable to W III, as it is for the calculations in Table 1.

In Fig. 2, a model spectrum of W I–III is plotted, which features line profiles broadened by a Gaussian kernel to produce a luminosity

Table 1. Luminosities for the 10 strongest lines from each W ion calculated at $T_e = 0.15$ eV, $n_e = 1 \times 10^6$ cm $^{-3}$, and a mass of 1×10^{-3} M $_{\odot}$. The atomic data used in the calculation of luminosities for these ions are from Smyth et al. (2018), Dunleavy et al. (2022), and McCann et al. (2024).

λ (nm)	Index ($i-j$)	E_i (cm $^{-1}$)	Lower i	E_j (cm $^{-1}$)	Upper j	$A_{j \rightarrow i}$ (s $^{-1}$)	Luminosity L (ph s $^{-1}$) (erg s $^{-1}$)	
W I lines								
5986.99	1–2	0.000	5p 6 5d 4 6s 2 5 D $_0$	1670.290	5p 6 5d 4 6s 2 5 D $_1$	5.32E–02	8.41E+49	2.79E+37
6041.42	2–4	1670.290	5p 6 5d 4 6s 2 5 D $_1$	3325.530	5p 6 5d 4 6s 2 5 D $_2$	1.27E–01	6.10E+49	2.01E+37
6646.86	4–5	3325.530	5p 6 5d 4 6s 2 5 D $_2$	4829.999	5p 6 5d 4 6s 2 5 D $_3$	1.35E–01	2.11E+49	6.31E+36
7197.71	5–6	4829.999	5p 6 5d 4 6s 2 5 D $_3$	6219.330	5p 6 5d 4 6s 2 5 D $_4$	9.28E–02	5.09E+48	1.41E+36
1272.63	2–7	1670.290	5p 6 5d 4 6s 2 5 D $_1$	9528.058	5p 6 5d 4 6s 2 3 P $_0$	8.07E+00	1.14E+47	1.79E+35
3059.94	3–6	2951.289	5p 6 5d 5 6s 7 S $_3$	6219.330	5p 6 5d 4 6s 2 5 D $_4$	2.33E–03	1.28E+47	8.31E+34
1682.76	6–8	6219.330	5p 6 5d 4 6s 2 5 D $_4$	12 161.954	5p 6 5d 4 6s 2 3 H $_4$	1.33E+00	3.05E+46	3.61E+34
1001.85	4–9	3325.530	5p 6 5d 4 6s 2 5 D $_2$	13 307.096	5p 6 5d 4 6s 2 3 P $_1$	5.72E+00	8.45E+45	1.68E+34
1173.91	5–10	4829.999	5p 6 5d 4 6s 2 5 D $_3$	13 348.555	5p 6 5d 4 6s 2 3 G $_3$	1.66E+00	9.74E+45	1.65E+34
1363.89	5–8	4829.999	5p 6 5d 4 6s 2 5 D $_3$	12 161.954	5p 6 5d 4 6s 2 3 H $_4$	3.45E–01	7.92E+45	1.16E+34
W II lines								
6584.02	1–2	0.000	5p 6 5d 4 6s 6 D $_{1/2}$	1518.829	5p 6 5d 4 6s 6 D $_{3/2}$	2.06E–01	2.95E+50	8.90E+37
6047.25	2–3	1518.829	5p 6 5d 4 6s 6 D $_{3/2}$	3172.472	5p 6 5d 4 6s 6 D $_{5/2}$	2.80E–01	1.00E+50	3.29E+37
6477.50	3–4	3172.472	5p 6 5d 4 6s 6 D $_{5/2}$	4716.278	5p 6 5d 4 6s 6 D $_{7/2}$	1.86E–01	2.22E+49	6.80E+36
6989.07	4–5	4716.278	5p 6 5d 4 6s 6 D $_{7/2}$	6147.084	5p 6 5d 4 6s 6 D $_{9/2}$	8.60E–02	3.80E+48	1.08E+36
1367.26	2–8	1518.829	5p 6 5d 4 6s 6 D $_{3/2}$	8832.727	5p 6 5d 4 6s 4 P $_{1/2}$	2.81E+00	5.61E+47	8.16E+35
1132.15	1–8	0.000	5p 6 5d 4 6s 6 D $_{1/2}$	8832.727	5p 6 5d 4 6s 4 P $_{1/2}$	1.26E+00	2.51E+47	4.42E+35
1347.66	1–6	0.000	5p 6 5d 4 6s 6 D $_{1/2}$	7420.260	5p 6 5d 5 6 S $_{5/2}$	2.21E–02	2.30E+47	3.39E+35
1347.71	3–9	3172.472	5p 6 5d 4 6s 6 D $_{5/2}$	10 592.484	5p 6 5d 4 6s 4 P $_{3/2}$	7.06E–01	1.68E+47	2.48E+35
1694.50	2–6	1518.829	5p 6 5d 4 6s 6 D $_{3/2}$	7420.260	5p 6 5d 5 6 S $_{5/2}$	1.93E–02	2.01E+47	2.36E+35
1805.45	3–7	3172.472	5p 6 5d 4 6s 6 D $_{5/2}$	8711.273	5p 6 5d 3 6s 2 4 F $_{3/2}$	2.74E–02	6.50E+46	7.16E+34
W III lines								
4432.23	1–2	0.000	5p 6 5d 4 5 D $_0$	2256.199	5p 6 5d 4 5 D $_1$	5.04E–01	2.73E+50	1.22E+38
4535.16	2–3	2256.199	5p 6 5d 4 5 D $_1$	4461.194	5p 6 5d 4 5 D $_2$	5.40E–01	4.61E+49	2.02E+37
5504.75	3–4	4461.194	5p 6 5d 4 5 D $_2$	6277.808	5p 6 5d 4 5 D $_3$	2.60E–01	6.93E+48	2.50E+36
1307.51	2–6	2256.199	5p 6 5d 4 5 D $_1$	9904.296	5p 6 5d 4 3 P $_0$	6.98E+00	2.21E+47	3.37E+35
7097.87	4–5	6277.808	5p 6 5d 4 5 D $_3$	7686.681	5p 6 5d 4 5 D $_4$	7.13E–02	9.06E+47	2.54E+35
1536.73	3–7	4461.194	5p 6 5d 4 5 D $_2$	10 968.537	5p 6 5d 3 6s 5 F $_1$	1.35E–01	4.52E+46	5.85E+34
1187.67	3–9	4461.194	5p 6 5d 4 5 D $_2$	12 881.030	5p 6 5d 4 3 P $_1$	3.60E+00	3.16E+46	5.29E+34
804.69	1–8	0.000	5p 6 5d 4 5 D $_0$	12 427.091	5p 6 5d 3 6s 5 F $_2$	9.31E–02	1.13E+46	2.78E+34
1662.71	5–10	7686.681	5p 6 5d 4 5 D $_4$	13 700.943	5p 6 5d 4 3 H $_4$	6.07E–01	1.80E+46	2.16E+34
1147.80	2–7	2256.199	5p 6 5d 4 5 D $_1$	10 968.537	5p 6 5d 3 6s 5 F $_1$	3.00E–02	1.00E+46	1.74E+34

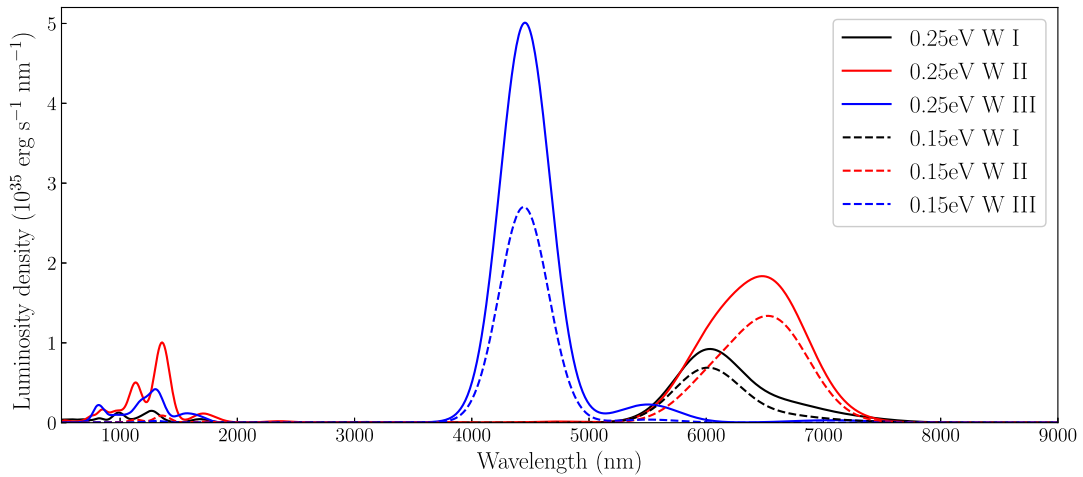
**Figure 2.** Luminosity density plot as a function of wavelength (nm) for W I–III generated at $T_e = 0.15/0.25$ eV, $n_e = 1 \times 10^6$ cm $^{-3}$, and a mass of 1×10^{-3} M $_{\odot}$.

Table 2. Luminosities for the 10 strongest lines from each Au ion calculated at $T_e = 0.15$ eV, $n_e = 1 \times 10^6$ cm $^{-3}$, and a mass of 1×10^{-3} M_\odot . The atomic data used in the calculation of luminosities for these ions are from McCann et al. (2022).

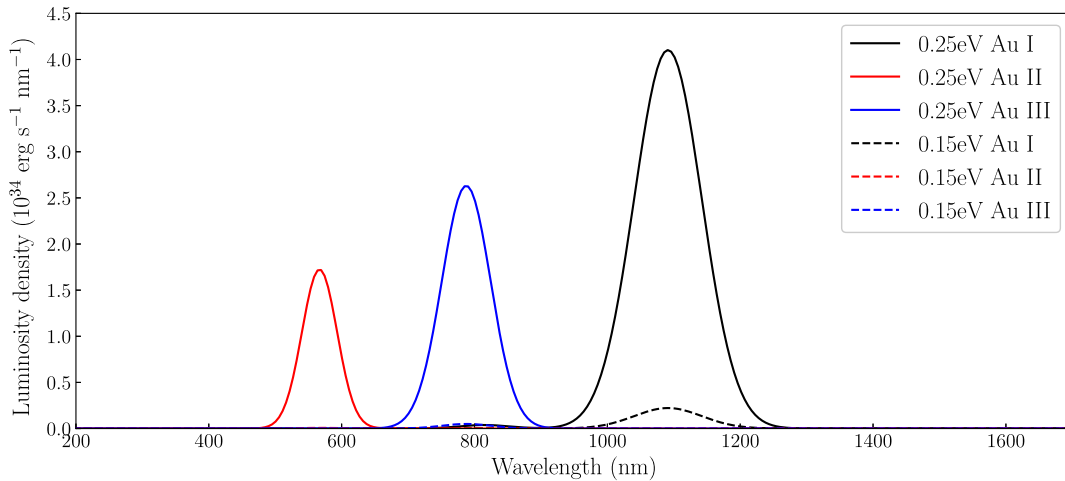
λ (nm)	Index ($i-j$)	E_i (cm $^{-1}$)	Lower i	E_j (cm $^{-1}$)	Upper j	$A_{j \rightarrow i}$ (s $^{-1}$)	Luminosity L (ph s $^{-1}$)	Luminosity L (erg s $^{-1}$)
Au I lines								
1091.56	1–2	0.000	5d 10 6s 2 S $_{1/2}$	9161.176	5d 9 6s 2 D $_{5/2}$	2.48E–02	1.56E+47	2.84E+35
814.73	2–3	9161.176	5d 9 6s 2 D $_{5/2}$	21 435.184	5d 9 6s 2 D $_{3/2}$	2.98E+01	1.76E+43	4.30E+31
466.52	1–3	0.000	5d 10 6s 2 S $_{1/2}$	21 435.184	5d 9 6s 2 D $_{3/2}$	1.31E+00	7.75E+41	3.30E+30
267.67	1–4	0.000	5d 10 6s 2 S $_{1/2}$	37 358.988	5d 10 6p 2 P $_{1/2}$	1.61E+08	2.70E+37	2.01E+26
242.87	1–5	0.000	5d 10 6s 2 S $_{1/2}$	41 174.609	5d 10 6p 2 P $_{3/2}$	2.26E+08	1.29E+36	1.06E+25
303.01	2–6	9161.176	5d 9 6s 2 D $_{5/2}$	42 163.529	5d 9 6s6p 4 P $_{5/2}$	1.37E+05	7.50E+35	4.92E+24
627.99	3–4	21 435.184	5d 9 6s 2 D $_{3/2}$	37 358.988	5d 10 6p 2 P $_{1/2}$	2.33E+06	3.91E+35	1.24E+24
312.37	2–5	9161.176	5d 9 6s 2 D $_{5/2}$	41 174.609	5d 10 6p 2 P $_{3/2}$	2.60E+07	1.49E+35	9.46E+23
274.91	2–7	9161.176	5d 9 6s 2 D $_{5/2}$	45 537.183	5d 9 6s6p 4 F $_{7/2}$	1.43E+06	8.34E+34	6.04E+23
268.69	2–9	9161.176	5d 9 6s 2 D $_{5/2}$	46 379.043	5d 9 6s6p 4 D $_{5/2}$	1.21E+06	1.89E+34	1.40E+23
Au II lines								
566.87	1–3	0.000	5p 6 5d 10 1 S $_0$	17 640.611	5p 6 5d 9 6s 3 D $_2$	4.05E–01	1.43E+45	5.03E+33
3844.62	2–3	15 039.574	5p 6 5d 9 6s 3 D $_3$	17 640.611	5p 6 5d 9 6s 3 D $_2$	2.87E–01	1.02E+45	5.26E+32
987.64	3–4	17 640.611	5p 6 5d 9 6s 3 D $_2$	27 765.754	5p 6 5d 9 6s 3 D $_1$	2.72E+01	1.97E+41	3.96E+29
685.79	2–5	15 039.574	5p 6 5d 9 6s 3 D $_3$	29 621.247	5p 6 5d 9 6s 1 D $_2$	2.71E+01	5.63E+40	1.63E+29
337.60	1–5	0.000	5p 6 5d 10 1 S $_0$	29 621.247	5p 6 5d 9 6s 1 D $_2$	8.27E+00	1.72E+40	1.01E+29
834.68	3–5	17 640.611	5p 6 5d 9 6s 3 D $_2$	29 621.247	5p 6 5d 9 6s 1 D $_2$	1.74E+00	3.61E+39	8.61E+27
785.78	2–4	15 039.574	5p 6 5d 9 6s 3 D $_3$	27 765.754	5p 6 5d 9 6s 3 D $_1$	4.98E–03	3.60E+37	9.11E+25
5389.40	4–5	27 765.754	5p 6 5d 9 6s 3 D $_1$	29 621.247	5p 6 5d 9 6s 1 D $_2$	5.42E–02	1.13E+38	4.15E+25
393.09	2–6	15 039.574	5p 6 5d 9 6s 3 D $_3$	40 478.743	5p 6 5d 8 6s 2 3 F $_4$	5.34E+00	7.08E+36	3.58E+25
497.86	3–6	17 640.611	5p 6 5d 9 6s 3 D $_2$	40 478.743	5p 6 5d 8 6s 2 3 F $_4$	7.39E–01	9.80E+35	4.45E+24
Au III lines								
787.77	1–2	0.000	5d 9 2 D $_{5/2}$	12 694.038	5d 9 2 D $_{3/2}$	3.30E+01	1.82E+46	4.60E+34
336.09	1–3	0.000	5d 9 2 D $_{5/2}$	29 753.996	5d 8 6s 4 F $_{9/2}$	1.34E–01	7.04E+39	4.17E+28
285.09	1–4	0.000	5d 9 2 D $_{5/2}$	35 076.856	5d 8 6s 4 F $_{7/2}$	1.05E+01	1.95E+38	1.36E+27
1878.69	3–4	29 753.996	5d 8 6s 4 F $_{9/2}$	35 076.856	5d 8 6s 4 F $_{7/2}$	3.72E+00	6.91E+37	7.31E+25
257.58	1–5	0.000	5d 9 2 D $_{5/2}$	38 822.353	5d 8 6s 4 F $_{5/2}$	7.95E+00	4.56E+36	3.52E+25
247.86	1–6	0.000	5d 9 2 D $_{5/2}$	40 345.844	5d 8 6s 4 F $_{3/2}$	2.04E+01	8.92E+35	7.15E+24
382.73	2–5	12 694.038	5d 9 2 D $_{3/2}$	38 822.353	5d 8 6s 4 F $_{5/2}$	1.09E+00	6.25E+35	3.25E+24
446.77	2–4	12 694.038	5d 9 2 D $_{3/2}$	35 076.856	5d 8 6s 4 F $_{7/2}$	2.78E–02	5.16E+35	2.30E+24
2669.87	4–5	35 076.856	5d 8 6s 4 F $_{7/2}$	38 822.353	5d 8 6s 4 F $_{5/2}$	1.01E+00	5.79E+35	4.31E+23
225.09	1–7	0.000	5d 9 2 D $_{5/2}$	44 425.917	5d 8 6s 4 F $_{5/2}$	1.72E+01	1.86E+34	1.65E+23

density spectrum. A full width at half-maximum (FWHM) of 0.11c (Gillanders & Smartt 2024) was assumed for all lines. The kernels are normalized such that an integral over each line gives the total luminosity specified in Table 1. The spectrum is calculated at $n_e = 1.0 \times 10^6$ cm $^{-3}$ for two different electron temperatures roughly representative of nebular KN events. To investigate blending between the ions' spectra, each ion is treated separately. Evidently the strongest feature is that of the two W III lines at 4.5 μ m. Notably, at these broadening parameters these two lines present themselves as essentially a single Gaussian feature. At a similar mass, it is found again that the W I and W II lines at around 6.05 μ m are of comparable strength. Additionally, there will be considerable blending between these two ion stages due to the overlap of the Gaussian profiles as seen in Fig. 2. None the less, it is feasible that future *JWST* observations could reach these large wavelengths in the IR, and in principle observe features here. This combined with the proposed W III identification may provide conclusive evidence of the element W in future KN-like events.

Recent **R**-matrix calculations by McCann et al. (2022), Bromley et al. (2023), and Gillanders et al. (2021) have provided new radiative and collisional excitation atomic data for the first three ionization stages of Pt and Au. To check for any additional potential sources of KN emission from these species, the photon luminosity calculations are repeated for Pt I–III and Au I–III using these new atomic data. In Table 2, the calculated luminosities in units ph s $^{-1}$ and erg s $^{-1}$ for the strongest 10 lines of each Au ion species are presented, and in Table 3 the corresponding values for the three Pt ions. Again the photon luminosities are computed with a reference mass of 10^{-3} M_\odot , an electron temperature $T_e = 0.15$ eV, and an electron density $n_e = 10^6$ cm $^{-3}$. Clearly, the luminosity strengths, for all six ions of both Au and Pt, are orders of magnitude lower than those predicted for W in Table 1, but the strongest transitions are similarly those among the low-lying levels. For completeness in Figs 3 and 4, the corresponding broadened luminosity density profiles as a function of wavelength are plotted, to visually display these strong features. Given the lack of discernible features at these wavelengths at the late

Table 3. Luminosities for the 10 strongest lines from each Pt ion calculated at $T_e = 0.15$ eV, $n_e = 1 \times 10^6$ cm $^{-3}$, and a mass of 1×10^{-3} M $_{\odot}$. The atomic data used in the calculation of luminosities for these ions are from Bromley et al. (2023).

λ (nm)	Index ($i-j$)	E_i (cm $^{-1}$)	Lower i	E_j (cm $^{-1}$)	Upper j	$A_{j \rightarrow i}$ (s $^{-1}$)	Luminosity L (ph s $^{-1}$)	(erg s $^{-1}$)
Pt I lines								
1522.66	1-5	0.000	5p 6 5d 9 6s 3 D $_3$	6567.450	5p 6 5d 9 6s 3 D $_2$	4.21E+00	2.46E+48	3.22E+36
12 888.66	1-2	0.000	5p 6 5d 9 6s 3 D $_3$	775.876	5p 6 5d 9 6s 1 D $_2$	3.26E-03	3.64E+48	5.62E+35
1076.07	3-6	823.661	5p 6 5d 8 6s 2 3 F $_4$	10 116.715	5p 6 5d 8 6s 2 3 F $_3$	2.01E+01	7.65E+46	1.41E+35
1726.65	2-5	775.876	5p 6 5d 9 6s 1 D $_2$	6567.450	5p 6 5d 9 6s 3 D $_2$	1.13E-01	6.61E+46	7.62E+34
1068.83	2-7	775.876	5p 6 5d 9 6s 1 D $_2$	10 131.867	5p 6 5d 9 6s 3 D $_1$	9.29E+00	2.57E+46	4.79E+34
1864.18	2-4	775.876	5p 6 5d 9 6s 1 D $_2$	6140.170	5p 6 5d 10 1 S $_0$	1.39E-02	2.75E+46	2.94E+34
740.95	1-8	0.000	5p 6 5d 9 6s 3 D $_3$	13 496.261	5p 6 5d 9 6s 1 D $_2$	7.74E+00	3.85E+45	1.03E+34
1070.57	2-6	775.876	5p 6 5d 9 6s 1 D $_2$	10 116.715	5p 6 5d 8 6s 2 3 F $_3$	9.81E-01	3.73E+45	6.94E+33
2805.51	5-7	6567.450	5p 6 5d 9 6s 3 D $_2$	10 131.867	5p 6 5d 9 6s 3 D $_1$	1.07E+00	2.96E+45	2.10E+33
1741.01	3-5	823.661	5p 6 5d 8 6s 2 3 F $_4$	6567.450	5p 6 5d 9 6s 3 D $_2$	2.48E-03	1.45E+45	1.66E+33
Pt II lines								
2188.35	2-4	4786.652	5p 6 5d 8 6s 4 F $_{9/2}$	9356.315	5p 6 5d 8 6s 4 F $_{7/2}$	2.54E+00	1.10E+48	1.00E+36
1187.67	1-3	0.000	5p 6 5d 9 2 D $_{5/2}$	8419.839	5p 6 5d 9 2 D $_{3/2}$	9.05E+00	5.02E+47	8.40E+35
1068.80	1-4	0.000	5p 6 5d 9 2 D $_{5/2}$	9356.315	5p 6 5d 8 6s 4 F $_{7/2}$	1.10E-01	4.77E+46	8.87E+34
2517.02	4-5	9356.315	5p 6 5d 8 6s 4 F $_{7/2}$	13 329.274	5p 6 5d 8 6s 4 F $_{5/2}$	1.96E+00	1.22E+46	9.65E+33
633.26	1-6	0.000	5p 6 5d 9 2 D $_{5/2}$	15 791.307	5p 6 5d 8 6s 4 F $_{3/2}$	3.85E+00	8.20E+44	2.57E+33
2036.89	3-5	8419.839	5p 6 5d 9 2 D $_{3/2}$	13 329.274	5p 6 5d 8 6s 4 F $_{5/2}$	2.68E-01	1.67E+45	1.63E+33
2089.14	1-2	0.000	5p 6 5d 9 2 D $_{5/2}$	4786.652	5p 6 5d 8 6s 4 F $_{9/5}$	6.17E-06	1.16E+45	1.10E+33
1339.65	4-7	9356.315	5p 6 5d 8 6s 4 F $_{7/2}$	16 820.928	5p 6 5d 8 6s 4 P $_{5/2}$	6.46E+00	6.38E+44	9.47E+32
751.25	2-8	4786.652	5p 6 5d 8 6s 4 F $_{9/2}$	18 097.766	5p 6 5d 8 6s 2 F $_{7/2}$	1.52E+01	3.48E+44	9.20E+32
750.23	1-5	0.000	5p 6 5d 9 2 D $_{5/2}$	13 329.274	5p 6 5d 8 6s 4 F $_{5/2}$	3.93E-02	2.45E+44	6.49E+32
Pt III lines								
1025.46	1-3	0.000	5d 8 3 F $_4$	9751.700	5d 8 3 D $_3$	4.66E+01	3.15E+47	6.10E+35
1126.28	2-4	5293.100	5d 8 1 D $_2$	14 171.896	5d 8 3 F $_2$	2.22E+01	5.22E+45	9.22E+33
2242.86	2-3	5293.100	5d 8 1 D $_2$	9751.700	5d 8 3 D $_3$	1.13E+00	7.63E+45	6.76E+33
870.44	2-6	5293.100	5d 8 1 D $_2$	16 781.599	5d 8 3 P $_1$	2.10E+01	3.68E+44	8.41E+32
2262.34	3-4	9751.700	5d 8 3 D $_3$	14 171.896	5d 8 3 F $_2$	3.05E+00	7.17E+44	6.31E+32
468.81	1-7	0.000	5d 8 3 F $_4$	21 330.798	5d 8 1 G $_4$	1.91E+01	1.38E+43	5.87E+31
3831.85	4-6	14 171.896	5d 8 3 F $_2$	16 781.599	5d 8 3 P $_1$	4.05E-01	7.10E+42	3.68E+30
863.63	3-7	9751.700	5d 8 3 D $_3$	21 330.798	5d 8 1 G $_4$	1.94E+00	1.41E+42	3.24E+30
457.94	1-8	0.000	5d 8 3 F $_4$	21 836.696	5d 7 6s 5 F $_5$	1.02E-02	3.94E+41	1.71E+30
5427.12	5-6	14 938.999	5d 8 3 P $_0$	16 781.599	5d 8 3 P $_1$	2.00E-01	3.51E+42	1.28E+30

**Figure 3.** Luminosity density plot as a function of wavelength (nm) for Au I-III generated at $T_e = 0.15/0.25$ eV, $n_e = 1 \times 10^6$ cm $^{-3}$, and a mass of 1×10^{-3} M $_{\odot}$.

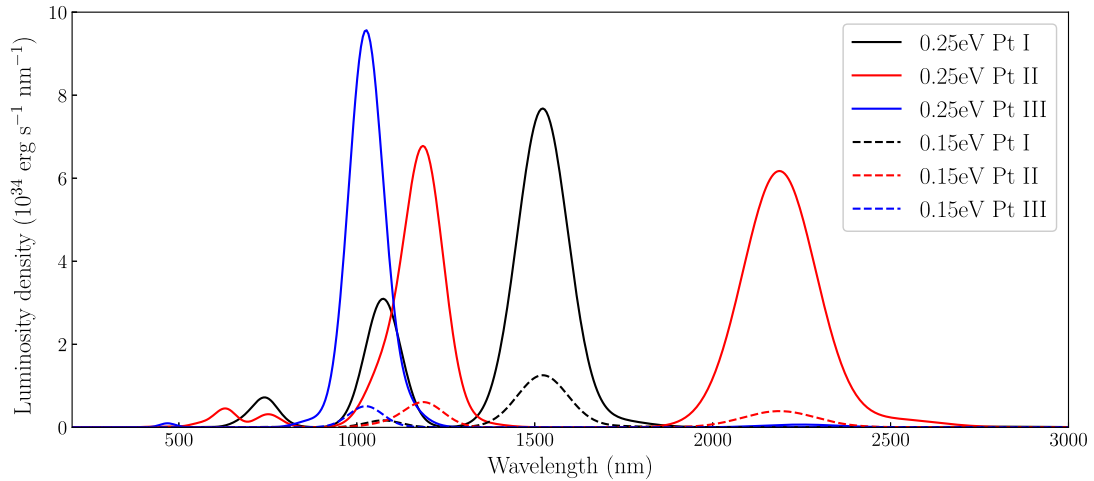


Figure 4. Luminosity density plot as a function of wavelength (nm) for Pt I–III generated at $T_e = 0.15/0.25$ eV, $n_e = 1 \times 10^6$ cm $^{-3}$, and a mass of $1 \times 10^{-3} M_\odot$.

times of AT2017gfo and AT2023vfi for Pt and Au, this places weak constraints on the masses of these elements as previously stated by Gillanders et al. (2021). It is therefore the case that higher quality observed data are required to make more conclusive estimates of the presence of the elements in future KN events, in addition to accurate theoretical data for representative species.

3.2 Ion-mass quantification for W

The late-time *Spitzer* observation (Villar et al. 2018; Kasliwal et al. 2019) of AT2017gfo and the observation of AT2023vfi (Levan et al. 2024) have produced interest in a potential feature at around 4.5 μ m. The ions W III and Se III both have thermally accessible fine-structure lines at around this wavelength. A first analysis was performed by Hotokezaka et al. (2022) using distorted-wave collision data calculated using the HULLAC code (Bar-Shalom et al. 2001). Here, a revised analysis of the parameter space for W III using the newly published **R**-matrix collisional data of McCann et al. (2024) for AT2017gfo is presented, and additionally a new analysis for AT2023vfi. These new atomic data are expected to be more accurate at low temperatures due to the inclusion of resonances when calculating the collision strengths.

For AT2017gfo, the late-time *Spitzer* observation in the 4.5 μ m band at 43 d had a total luminosity of 2×10^{38} erg s $^{-1}$. It was suggested by Hotokezaka et al. (2022) that W III could contribute as much as 5×10^{37} erg s $^{-1}$ to this, where their model required a W III mass of $\sim 2.0 \times 10^{-4} M_\odot$, at a temperature of 3500 K and electron density of 10^6 cm $^{-3}$. Enforcing these parameters and this integrated luminosity, the revised **R**-matrix data of McCann et al. (2024) require a mass of $\sim 1.65 \times 10^{-4} M_\odot$ of W III. Note that this estimate is based on the sum of the luminosities of both the ground configuration ($5d^4 6s^2$) $^5D_0 \rightarrow ^5D_1$ (4.43 μ m) and $^5D_1 \rightarrow ^5D_2$ (4.54 μ m) transitions being 5×10^{37} erg s $^{-1}$. In this case, the mass predicted is in agreement with that of Hotokezaka et al. (2022). The good agreement between atomic data sets here shows that the limiting factor in making such an estimate are likely the observed data, and in particular what fraction of the *Spitzer* band to assign to this emission line. Additionally, certain limitations are introduced with the assignment of an electron temperature and density. This estimate represents an ejecta mass fraction of W III of around 0.33 per cent in AT2017gfo (assuming an ejecta mass of $5 \times 10^{-2} M_\odot$), and assuming a similar production of other ion stages’ results in

perhaps as much as 1.0 per cent of the ejecta being W. While there is good agreement with the calculations of Hotokezaka et al. (2022), it is important to note that the methods here are more general. The use of a full collisional radiative model allows for mass predictions in any electron density regime, as opposed to assuming a coronal or local thermodynamic equilibrium (LTE) approximation. Additionally, including resonances when calculating the collision strengths allows for more accurate predictions at low temperatures – where collision strengths could be underestimated using the distorted wave method.

For AT2023vfi, the feature has been integrated to have a specific luminosity of $\sim 1.0 \times 10^{38}$ erg s $^{-1}$ (Gillanders & Smartt 2024). Enforcing this luminosity, and a late-time electron density of $\sim 3 \times 10^5$ cm $^{-3}$ (Levan et al. 2024), at an electron temperature of 3000 K (Levan et al. 2024), the **R**-matrix data of McCann et al. (2024) require a W III mass of $\sim 9.4 \times 10^{-4} M_\odot$. As for AT2017gfo, this calculation is based on the sum of the 4.43 and 4.54 μ m transitions. Given a total ejecta mass of $6 \times 10^{-2} M_\odot$ (Levan et al. 2024), this mass of W III represents a fraction of around 1.6 per cent. Without a quantitative treatment of ionization fraction, an elemental mass is difficult to quantify. Assuming reasonably similar fractions for the near neutral stages of W, it is perhaps feasible that up to ~ 4.7 per cent could potentially be present in the ejecta.

Fig. 5 shows the synthetic W spectrum compared with the *JWST* spectrum of AT2023vfi (Levan et al. 2024). The centroid and width of the ~ 4.5 μ m feature was fitted by Gillanders & Smartt (2024), which is also shown in Fig. 5. The spectrum was produced using an electron temperature of 0.26 eV and an electron density of 3×10^5 cm $^{-3}$. A Gaussian kernel was again assumed with an FWHM of 0.110c (Gillanders & Smartt 2024). With a W III mass of $9.4 \times 10^{-4} M_\odot$, a good match to the *JWST* data can be found assuming a continuum of a power law added to a blackbody at 620 K. This blackbody temperature is in rough agreement with those suggested by Gillanders & Smartt (2024) and Levan et al. (2024).

The non-uniformity of the electron density and temperature makes the assignment of either quantity in simple models like this difficult. For this reason, an investigation is conducted across a wide range of temperature and density space to determine how the mass estimate varies subject to different conditions, in some sense accounting for a reasonable uncertainty in these quantities. This is shown in Fig. 6 for a range of luminosities centred at 1.0×10^{38} erg s $^{-1}$ to also investigate a rough uncertainty in the integration of the feature.

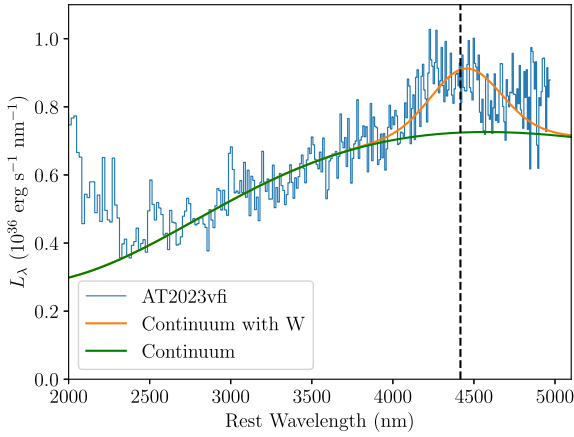


Figure 5. The calculated W III spectrum at $T_e = 0.26$ eV and $n_e = 3 \times 10^5$ cm^{-3} , with FWHM set to $0.110c = 486$ nm (Gillanders & Smartt 2024). A blackbody and power-law continuum is employed. This is overlaid on the *JWST* spectrum (Levan et al. 2024). The dashed black line shows the measured centroid of the line published by Gillanders & Smartt (2024).

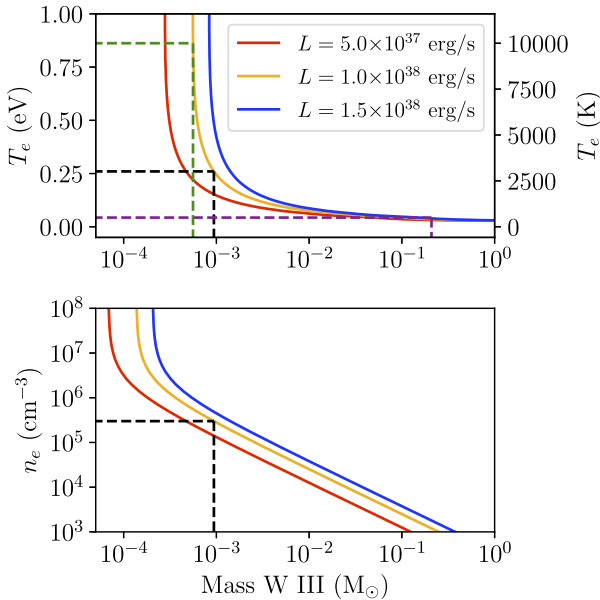


Figure 6. Contour plots of constant luminosity, at values of $L = 5.0 \times 10^{37}$ erg s^{-1} , $L = 1.0 \times 10^{38}$ erg s^{-1} , and $L = 1.5 \times 10^{38}$ erg s^{-1} . The parameter space of W III mass, electron temperature, and electron density are explored. On the top panel, the density is fixed at 3×10^5 cm^{-3} . The dashed lines are fixed electron temperatures, namely 500 K (0.04 eV, purple), 3000 K (0.26 eV, black), and 10000 K (0.86 eV, green). On the bottom panel, the electron temperature is fixed at 0.26 eV. The black dashed line is a constant density of 3×10^5 cm^{-3} .

At a fixed temperature, the density and mass required to produce a fixed luminosity are inversely proportional in the limit of low density. This is simply a manifestation of the coronal regime of the collisional radiative equations. In contrast, the high density limit naturally requires less and less mass of W III to produce the features.

With increasing temperature at fixed density it is naturally found that less mass of W III is required to produce the feature. The green dashed line on the top panel of Fig. 6 shows the implications of a temperature of 0.86 eV (temperatures this high have been suggested by the models of Pognan, Jerkstrand & Gruner 2022). In this

case, a relatively low mass of $5.6 \times 10^{-4} M_\odot$ of W III is required to produce the feature. However, at such temperatures significant emission should begin to appear in the ~ 1.0 – 1.8 μm range from W II and W III and at around ~ 0.5 μm from W I, as shown in Fig. 7. While this in principle could constrain the mass of W I, the excess emission expected from W III that is not present in the observation perhaps prevents this from being a valid identification. In summary, for W III to be responsible for the excess flux at around ~ 4.5 μm at the rough density regime of $\sim 10^5$ cm^{-3} , it is required that the electron temperature also remains relatively low at around say 2500 K. Conversely, at low electron temperatures, say at around the ~ 500 K blackbody temperatures reported by Gillanders & Smartt (2024) and Levan et al. (2024), the feature requires unreasonably high masses of around $2.1 \times 10^{-1} M_\odot$ of W III.

4 IMPLICATIONS OF THE LIMITS ON THE EJECTED MASS OF W

In this section, we compare theoretical merger models based on hydrodynamical simulations and nuclear network calculations with the estimated masses of W III derived in the previous section, i.e. $1.65 \times 10^{-4} M_\odot$ for AT2017gfo and $9.4 \times 10^{-4} M_\odot$ for AT2023vfi. Observational uncertainties of these estimates are discussed in the previous section, e.g. assumptions about the temperature and the possibility of line blending. The merger models only provide the total amount of W without distinguishing different ionization states and are themselves connected with uncertainties, some of which are briefly addressed below. Despite these uncertainties, this comparison reveals a broad consistency between theoretical predictions and the observations and highlights the particular usefulness of W measurements to constrain the properties of the merger outflow and the abundance of other elements.

In Table 4, we list the results from a selection of neutron star merger models, drawn from Just et al. (2023) and Sneppen et al. (2024), which strive for a complete and consistent description of *all* mass ejection channels. The set consists of four models taken from Just et al. (2023), two for equal-mass binaries (‘sym’) and two with a binary mass ratio of $q = 0.75$ (‘asy’). In order to capture the effects of turbulent angular momentum transport during the post-merger evolution, these models adopt a viscosity model (Shakura & Sunyaev 1973). For each of the aforementioned two cases, we consider one model with a fairly strong (‘n1-a6’) and one model with relatively weak (‘n10-a3’) viscosity. The models of Just et al. (2023) only involve relatively long-lived neutron star remnants that collapse ~ 100 ms after merger or later (cf. τ_{BH} in Table 4). We supplement these with two models (one equal-mass and one asymmetric) from Sneppen et al. (2024) having short-lived remnants (i.e. collapsing at 10 ms after merger, labelled ‘short’; see references for details). The simulations consider neutron stars with masses comparable to those in AT2017gfo. The total amount of ejecta in these simulations is also broadly consistent with the estimated total ejecta mass of AT2017gfo, namely about 0.03 – $0.05 M_\odot$ (e.g. Smartt et al. 2017). In addition to the initial binary parameters and merger dynamics, nucleosynthesis yields are also affected by nuclear physics uncertainties, which are particularly significant for heavy, neutron-rich nuclei. To explore this sensitivity, we add two further models that adopt the DZ31 nuclear mass model (Duflo & Zuker 1995) compared to the models in Just et al. (2023) and Sneppen et al. (2024), which adopted the HFB21 model (Goriely, Chamel & Pearson 2010) as well as the consistently derived (n, γ) and (γ, n) rates in Mendoza-Temis et al. (2015). These two models are chosen to have all other simulation parameters

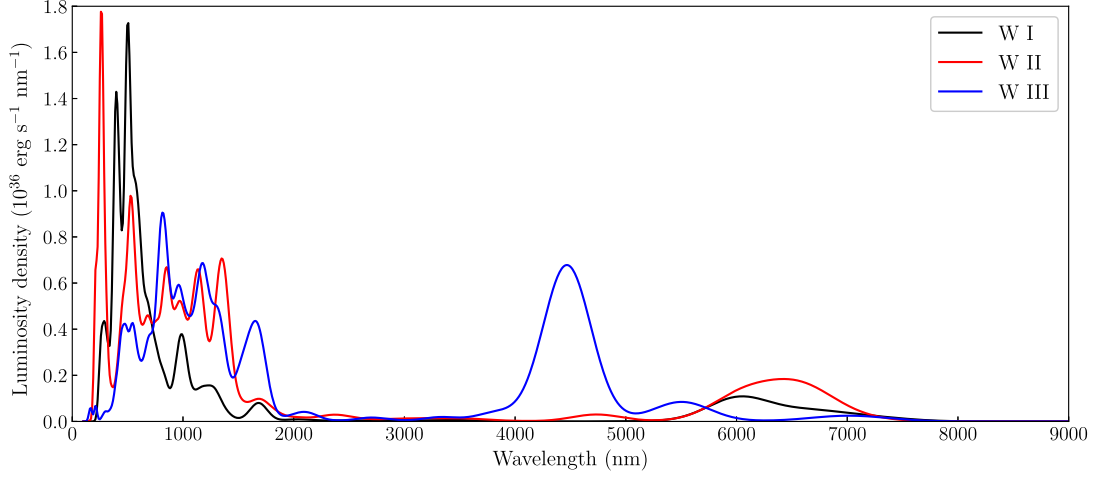


Figure 7. Luminosity density plot as a function of wavelength (nm) for W I–III generated at $T_e = 0.86$ eV, $n_e = 1 \times 10^6$ cm $^{-3}$, and a mass of 1×10^{-3} M_\odot .

Table 4. Ejecta masses and mass fractions in selected neutron star merger models of Just et al. (2023) and Sneppen et al. (2024). The second row lists the nuclear mass model employed for the nucleosynthesis post-processing of the ejecta, τ_{BH} denotes the time after merger when the neutron star remnant collapsed to a black hole, M_{tot} is the total ejecta mass, $M(W, 1 \text{ mth})$ and $M(W, 1 \text{ Gyr})$ are the total W masses 1 month and 1 billion years after the merger, respectively, $M(Y_e < 0.2)$ is the total amount of ejecta with electron fractions Y_e below 0.2 at 5 GK, $X(W, 1 \text{ mth})$ is the mass fraction of W 1 month after merger, and the last row provides the ratio between the W mass at 1 month and ejecta mass with $Y_e < 0.2$. Numbers are given with the notation $A(B) := A \times 10^B M_\odot$.

Merger simulation	sym-n1-a6	sym-n10-a3	asy-n1-a6	asy-n10-a3	sym-n1-a6-short	asy-n1-a6-short	sym-n1-a6	asy-n1-a6-short
Nuclear mass model	HFB21	HFB21	HFB21	HFB21	HFB21	HFB21	DZ31	DZ31
τ_{BH} (ms)	122	915	96	680	10	10	122	10
M_{tot} (M_\odot)	7.35(−2)	3.25(−2)	8.63(−2)	6.13(−2)	1.16(−2)	2.44(−2)	7.35(−2)	2.44(−2)
$M(W, 1 \text{ mth})$ (M_\odot)	5.57(−5)	5.46(−5)	6.96(−5)	6.88(−5)	4.51(−5)	8.13(−5)	1.63(−4)	2.46(−4)
$M(W, 1 \text{ Gyr})$ (M_\odot)	3.40(−5)	3.30(−5)	4.30(−5)	4.19(−5)	2.75(−5)	4.99(−5)	1.15(−4)	1.77(−4)
$M(Y_e < 0.2)$ (M_\odot)	2.08(−3)	2.05(−3)	2.94(−3)	3.11(−3)	1.54(−3)	3.74(−3)	2.08(−3)	3.74(−3)
$X(W, 1 \text{ mth})$	0.08 per cent	0.17 per cent	0.08 per cent	0.11 per cent	0.39 per cent	0.33 per cent	0.22 per cent	1.01 per cent
$\frac{M(W, 1 \text{ mth})}{M(Y_e < 0.2)}$	2.68 per cent	2.66 per cent	2.37 per cent	2.21 per cent	2.93 per cent	2.17 per cent	7.84 per cent	6.58 per cent

matching previous cases such that the influence of changing the nuclear physics input alone can be ascertained.

Elemental abundances in a KN are generally time dependent, because the radioactive decay half-lives are comparable to the relevant observable time-scales of hours to months. The dominating decay mode, beta decay, maintains constant the isotopic abundances but modifies the elemental abundances. To exemplify this, we show in Fig. 8 the time evolution of the relative W mass fraction $X(W)$ resulting in the simulation ‘sym-n1-a6’ with the HFB21 nuclear mass model along with the contributions from individual isotopes. At around 1 d, ^{187}W decays, and the total mass fraction decreases. The decays of the other two isotopes ^{188}W and ^{185}W (with half-lives of around 70 and 75 d, respectively) lead to a further reduction (see supplemental material of Wu et al. 2019), despite a minor compensation from the decays of ^{184}Ta and ^{183}Ta . As a consequence, the mass fraction of W decreases by a factor of ~ 2 from the first hours to around 2 months after merger. Notice that this decrease should occur in any r -process model that reproduces the isotopic abundance pattern observed in the Solar system around the third r -process peak. Given that the observations of AT2017gfo and AT2023vfi discussed in Section 3.2 were taken at 43 and 29 d, respectively, after the merger, we base the following quantitative comparison on the mass fractions taken at 1 month, which are listed in Table 4.

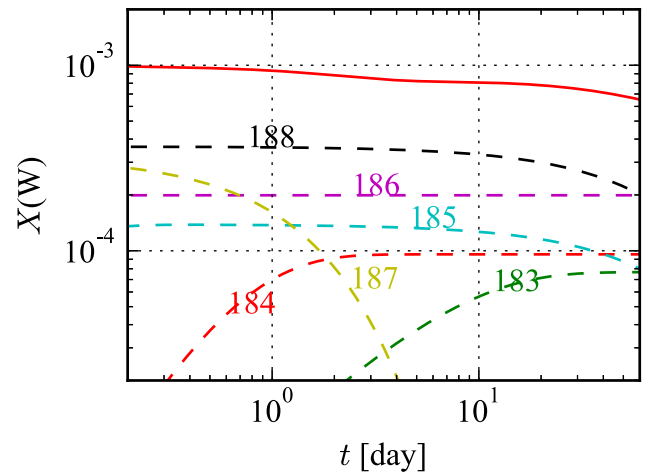


Figure 8. Time evolution of W mass fraction (solid red curve) from 0.2 to 60 d averaged over all ejecta in the sym-n1-a6-HFB21 model. The contributions from different W isotopes are shown by dashed curves labelled by their mass numbers. The decays of ^{187}W , ^{188}W , and ^{185}W lead to a moderate reduction of the total W abundance from ~ 0.1 d to ~ 1 month.

The predicted W masses scatter in the different merger models between 4×10^{-5} and $2 \times 10^{-4} M_{\odot}$ and are thus broadly consistent with the mass of W III derived through the luminosity of the 4.5 μm feature in the spectra of AT2017gfo and AT2023vfi, providing tentative evidence that the inference presented in Section 3.2 yields reasonable estimates. The agreement is particularly good for AT2017gfo. Although most of the models give W masses that are a factor of 2–3 smaller than our estimated $1.65 \times 10^{-4} M_{\odot}$ (cf. Section 3.2), the full spread within the models encompasses this value. Also, several of the simulations yield mass fractions for W, $X(\text{W})$, that are close to the estimated fraction of 0.3 per cent (Section 3.2). The short-lived merger models tend to yield somewhat higher values of $X(\text{W})$ in slightly better agreement with the mass fraction estimate from Section 3.2; however, the total ejecta masses in these models are slightly too small to be compatible with AT2017gfo. Considering AT2023vfi, the inferred W III mass of $\sim 9.4 \times 10^{-4} M_{\odot}$ is up to one order of magnitude in excess of what the simulations predict, which were, however, originally set up to reproduce AT2017gfo-like systems. At this point, we cannot judge whether this discrepancy is a deficiency of the approach adopted in this study keeping in mind, in particular, as noted in Section 3.2, that the ion mass inferred from observations may be an overestimate if line blending is occurring, or only an upper limit if the feature is dominated by another process. Alternatively, this discrepancy may originate from different physical properties of the outflow in AT2023vfi compared to AT2017gfo. As discussed below, a higher W mass points to more neutron-rich ejecta, which may result from a binary with different masses than AT2017gfo. Since the gravitational-wave signal of AT2023vfi was not detected, the binary masses in this event are unknown. High ejecta masses and very neutron-rich outflows may also result from a neutron star–black hole merger (e.g. Kyutoku, Shibata & Taniguchi 2021), which may also be a possible progenitor of AT2023vfi. The numbers in Table 4 also show very clearly that the nuclear physics input for the network calculation has a significant impact on the W production, with DZ31 yielding systematically higher W masses (compare columns 2 and 8 or columns 7 and 9, respectively). Other aspects such as beta decay and fission rates may also impact the final abundance yields. The uncertainties of the nuclear model may thus represent another possible contribution explaining the difference between the theoretically predicted abundance and the W III mass inferred from observations. Obviously, the current set of merger simulations is not exhaustive, and other physical ingredients (e.g. a different nuclear equation of state in the simulation) may yield different W masses. Moreover, due to their high level of complexity, the hydrodynamical simulations still adopt a number of approximations (e.g. in the neutrino transport and treatment of small-scale turbulence) and may not be fully resolved numerically.

In general, the *r*-process is only sufficiently strong to produce significant amounts of W under neutron-rich conditions, i.e. if the electron fraction Y_e characterizing the neutron-richness of the outflow is below 0.2–0.25. This is exemplified in Fig. 9, where we bin the mass fraction of W as a function of Y_e for the outflow tracer particles of four different merger models. Below $Y_e \approx 0.2$, the W mass fraction is roughly constant in all models. The total W mass over the total ejected mass with $Y_e < 0.2$ is given in Table 4, having similar values of ~ 2.5 per cent for HFB21 models and ~ 6 per cent for DZ31 models. The difference can be understood by looking at the behaviour of the double neutron separation energy, S_{2n} , in the region of progenitor nuclei of stable W with $A \sim 186$. In the solar *r*-process abundance pattern, W appears in the low-mass number tail of the third peak. Its progenitors are located just before the neutron shell closure at $N = 126$. In the DZ31 mass model, for an isotopic

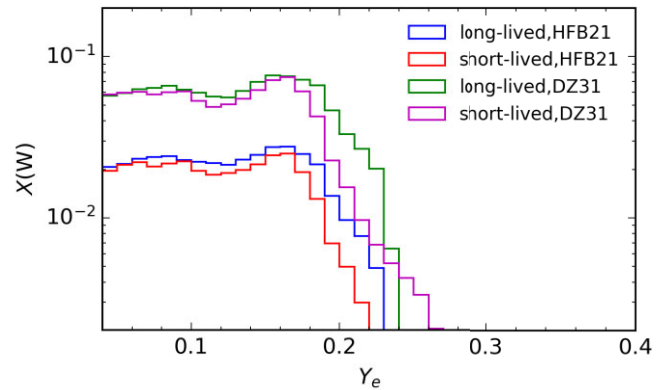


Figure 9. Histogram of W mass fraction measured at 1 month with respect to the electron fraction Y_e for models sym-n1-a6 and asy-n1-a6-short with HFB21 and DZ31 nuclear mass inputs. This figure adopts the electron fraction of the individual tracer particles when they reach a temperature of 5 GK.

chain the S_{2n} values decrease monotonically with respect to the mass number while they may become nearly constant or even increase in other models such as HFB21. In the latter case, the competition between neutron capture and photodissociation reactions produces a trough in the abundance pattern in the region where the progenitor nuclei of W are located (see e.g. Arcones & Martínez-Pinedo 2011).

The robust pattern for the ratio of the W mass to the total ejecta mass with $Y_e < 0.2$, $M(Y_e < 0.2)$, suggests the possibility to use a measured W mass as a proxy for the amount of neutron-rich ejecta, the theoretical prediction of which, however, is still affected by nuclear physics uncertainties. Based on the values from Table 4, neutron-rich material should roughly amount to about 40 times (14 times) the inferred W mass for HFB21 (DZ31), i.e. to $6.6 \times 10^{-3} M_{\odot}$ ($2.3 \times 10^{-3} M_{\odot}$) for AT2017gfo and to $2.8 \times 10^{-2} M_{\odot}$ ($9.8 \times 10^{-3} M_{\odot}$) for AT2023vfi. For this neutron-rich material, the measured W mass constrains the production of non-thermal electrons by beta decay. We find that for times later than a month ^{188}W represents the dominating contribution.

Potentially, a measured W mass fraction may provide a handle on the merger remnant lifetime since, within the set of simulations in Table 4, $X(\text{W})$ is systematically reduced for long-lived models, for which a neutrino-driven wind increases the contribution of less neutron-rich material (e.g. Perego et al. 2014; Lippuner et al. 2017; Fujibayashi et al. 2020; Just et al. 2023). This idea, however, requires more work to be solidified, as for instance model sym-n1-a6 with a low $X(\text{W})$ has a shorter lifetime than sym-n10-a3.

Given the tight connection between the W mass and the mass of ejecta with $Y_e < 0.2$, it is instructive to examine specific relationships between $X(\text{W})$ and selected classes of species produced by low- Y_e material. In particular, we address the extent to which $X(\text{W})$ can be used as a tracer for the amount of third-peak elements or of lanthanides and actinides. Fig. 10 shows the correlation of the W mass fraction with the mass fraction of all lanthanides and actinides, $X_{\text{La}} + X_{\text{Ac}}$, and the mass fraction of all third *r*-process peak elements, $X(\text{3rd peak})$, respectively. Adopting the integrated yields of the individual simulations listed in Table 4, the merger models for a given nuclear physics input (mass model) exhibit a very tight correlation implying that a measured mass fraction of W directly constrains the amount of lanthanides/actinides or of third-peak elements (as, for instance, gold and platinum). Employing different nuclear physics input apparently yields a roughly constant offset of this correlation. The solar abundance pattern leads to a similar, but

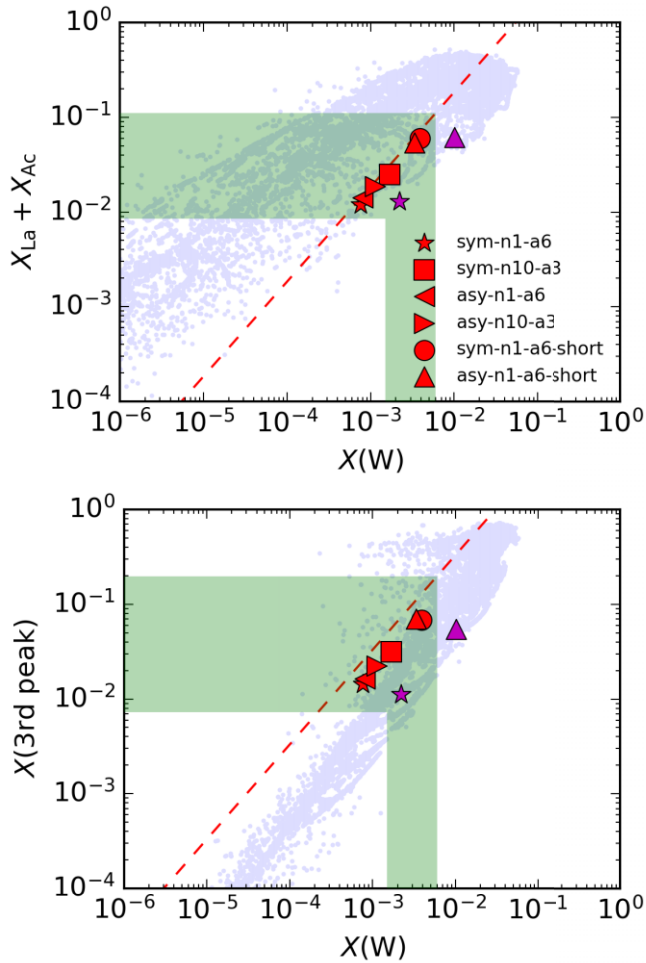


Figure 10. Correlation plots of W mass fraction with the total mass fraction of lanthanides and actinides, $X_{\text{La}} + X_{\text{Ac}}$ (upper panel), and with the mass fraction of third-peak r -process elements, $X(\text{3rd peak})$ (lower panel), for all models listed in Table 4 with red symbols for the HFB21 nuclear mass models and magenta markers for DZ31-based calculations. Red dashed lines display the ratio of mass fractions in solar r -process yields (Goriely 1999) with the W mass fraction converted to 1 month by including the presence of $^{185,188}\text{W}$ that eventually decay into ^{185}Re and ^{188}Os (for the variation of W mass fractions between 1 month and 1 Gyr, see Table 4; we do not convert lanthanide and third-peak mass fractions since the time dependence of averages over several elements and isotopes should be small). The actinide mass fraction is subdominant compared to lanthanides at 1 month. Light blue dots show the mass fraction for all individual tracer particles of the HFB21-based models. The vertical green band indicates our observational estimate of $X(\text{W}) \approx 0.3$ per cent, with an estimated uncertainty of a factor of 2 towards both sides. The horizontal green bands cover the corresponding ranges adopting the DZ31 models (for the lower limit) and the solar abundance pattern (for the upper limit).

slightly shifted relation, reflecting the fact that the merger models do not exactly reproduce the solar composition (see Just et al. 2023).

A W mass fraction of 0.3 per cent as estimated in Section 3.2 corresponds to a mass fraction 1.8 per cent $\lesssim X_{\text{La}} + X_{\text{Ac}} \lesssim 5.5$ per cent, where lanthanides dominate over actinides by far for the time-scales considered here. For the conversion, we adopt the relation between $X(\text{W})$ and $X_{\text{La}} + X_{\text{Ac}}$ for the solar abundance to estimate the upper limit, and we employ the data points of the DZ31 models to determine a linear relation, which provides the lower bound. We assume W III to be the dominant ionization state.

As an estimate of the uncertainties in the analysis and interpretation, which are typically a factor of a few (see Section 3.2), in Fig. 10 we show a green band corresponding to a factor of 2 variation in both directions and a horizontal green band illustrating the corresponding uncertainties in $X_{\text{La}} + X_{\text{Ac}}$ (using the same conversion as above). Despite the remaining uncertainties, our study suggests that a significant amount of lanthanides was produced in AT2017gfo and AT2023vfi. We note that our estimated range of the lanthanide mass fraction (neglecting the small contributions from actinides) is in good agreement with the mass fraction of lanthanides that, according to the analysis of Ji, Drout & Hansen (2019), would be required by the observations of metal-poor stars for mergers to represent the main source of r -process elements. Interestingly, the high lanthanide mass fractions that we find exceed most of the estimates made based on the light curve of AT2017gfo in the literature surveyed by Ji et al. (2019). Similarly, our work predicts that a sizable amount of third-peak r -process elements of about 1.6 per cent $\lesssim X(\text{3rd peak}) \lesssim 9.9$ per cent was co-produced (see lower panel of Fig. 10).

Although we assume that the integrated yields of the different models and the solar composition represent a reasonable range for characterizing the integrated outflows of merger events such as AT2017gfo, we overplot $X_{\text{La}} + X_{\text{Ac}}$ and $X(\text{W})$ for all tracer particles of the six HFB21 models in Fig. 10 (light blue dots) to visualize the local variation within the ejecta. The correlation between $X_{\text{La}} + X_{\text{Ac}}$ and $X(\text{W})$ is similar but not strictly linear with a larger spread of more than one order of magnitude in the mass fraction. As seen in Fig. 9, the mass fraction of W drops to zero when Y_e changes from 0.18 to 0.25, i.e. in a very narrow range. The dots at low $X(\text{W})$ originate from this transition region and do not exactly follow the $X(\text{W})$ – $(X_{\text{La}} + X_{\text{Ac}})$ correlation favouring the production of lanthanides. Visualizing the outcome of all tracers is likely overestimating the spread in the correlation because individual tracers may experience rather extreme conditions, which do not have a significant impact on the average behaviour and are thus not representative of any viable full merger model.

5 VELOCITY DISTRIBUTION

A further test of consistency between merger models and observations is to consider the velocity distribution of the ejected W in comparison to constraints on width of the observed spectral feature, which can be primarily attributed to Doppler broadening. Fig. 11 shows the distribution of ejected W mass versus radial velocity for four representative models from Table 4. In all these models, the W ejection velocity spans a fairly wide range, peaking around $\sim 0.2c$. There is a noticeable difference, however, in the amount of low-velocity ($< 0.1c$) W when comparing models with short-lived neutron star remnants to those with long-lived remnants (the wind from a long-lived remnant leads to inner ejecta that are relatively W-poor).

This difference in velocity distribution has implications for the expected profile shape, which, given spectroscopic observations of sufficient quality, provides further constraints on the models. To illustrate this, we have computed simple optically thin emission line profile shapes for the 4432.23 nm W III transition (Fig. 12) using the framework presented by Jerkstrand (2017), which is accurate to first order in v/c . For these calculations, we do not take into consideration any temperature/ionization variations in the ejecta, or any departures from spherical symmetry, and thus they should be considered only illustrative, pending more detailed modelling. The calculations assume that the emission is optically thin and that the

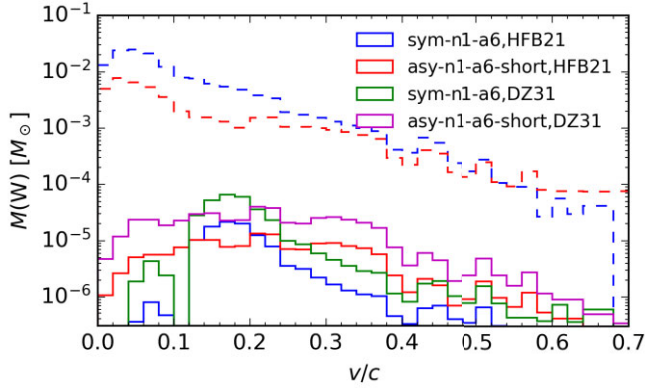


Figure 11. Histograms of W mass (solid lines) as a function of radial velocity for models sym-n1-a6 and asy-n1-a6-short with HFB21 and DZ31 nuclear mass inputs (plotted for composition at 1 mth post-merger). Dashed histograms show the total mass distributions, which are identical for our models that differ only in their nuclear mass inputs.

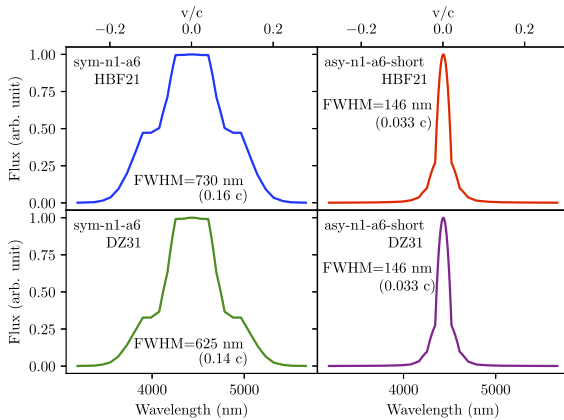


Figure 12. Line profile shapes computed from the W mass and total mass distributions for models sym-n1-a6 and asy-n1-a6-short with HFB21 and DZ31 nuclear mass models. Each profile is plotted for the 4432.23 nm W III line and normalized to peak. The FWHM is indicated for each case.

emissivity is proportional to the product of the W particle density and the total mass density (adopted as a proxy for the free-electron density, under the assumption of uniform ionization).

Despite the simplicity of the calculations, these profiles indicate the potential to obtain information on the distribution of W in the ejecta, and possibly the fate of the merger remnant, through KN observations. In particular, our models with short-lived neutron star remnants suggest narrow profiles, owing to the relatively high densities at low velocity. In contrast, the absence of W at low velocities leads to broad, somewhat flat topped profiles for our models with long-lived neutron star remnants. More sophisticated modelling is required to draw firm conclusions from comparisons with the observations of AT2023vfi, but these simple calculations suggest somewhat better compatibility of the short-lived remnant models with the relatively narrow observed profile (FWHM $\sim 0.11c$; Gillanders & Smartt 2024), although we note that the present calculation yields profiles that are somewhat too narrow. This may be indicative of line blending or a more extended velocity distribution, but more detailed modelling (involving temperature and ionization calculations) is needed to draw firm conclusions.

6 CONCLUSIONS

The available atomic data for W, Pt, and Au (Smyth et al. 2018; Dunleavy et al. 2022; McCann et al. 2022, 2024; Bromley et al. 2023) including transition rates and collision rates have been used to construct collisional radiative models, producing level populations for these ions under KN conditions. These data have subsequently been used to make luminosity predictions for the aforementioned ions (see Tables 1, 2, and 3). In this analysis, it is evident that the luminosities of the features in Pt and Au are, in general, orders of magnitude lower than those of W; however, this is when all the luminosities are calculated with the same $10^{-3} M_{\odot}$ mass. The blending of the features produced by these ions are also explored in Figs 2, 3, and 4, where the largest feature produced by the calculations at $4.5 \mu\text{m}$ is a mix of the 4432.23 and 4535.16 nm lines from the $5d^4 5D_0-5d^4 5D_1$ and $5d^4 5D_1-5d^4 5D_2$ transitions in W III.

The suggested luminosities from observations of the AT2017gfo and the AT2023vfi, from Hotokezaka et al. (2022) and Gillanders & Smartt (2024), respectively, have been used to determine mass estimates using the inverse procedure. Starting with the luminosity from observations, the required mass necessary to produce this value has been calculated using the available atomic data. For AT2017gfo, the measured luminosity was $5 \times 10^{37} \text{ erg s}^{-1}$, which resulted in a mass of $1.65 \times 10^{-4} M_{\odot}$. For AT2023vfi, the measured luminosity was $1.0 \times 10^{38} \text{ erg s}^{-1}$, which resulted in a mass of $9.4 \times 10^{-4} M_{\odot}$. A total ejecta mass of $5 \times 10^{-2} M_{\odot}$ for AT2017gfo from Hotokezaka et al. (2022) implies that ~ 0.33 per cent of the ejecta mass is W III, while for AT2023vfi a total ejecta mass of $6 \times 10^{-2} M_{\odot}$ from Levan et al. (2024) implies that ~ 1.6 per cent of the ejecta mass is W III. Assuming a similar amount of the first few ion stages, this analysis would predict that ~ 1.0 per cent of the AT2017gfo and ~ 4.7 per cent of the AT2023vfi are from W.

To test plausibility, the estimated amount of W III is compared with the results from theoretical models of matter outflows of neutron star mergers based on hydrodynamical simulations and nuclear network calculations. These models, which resemble AT2017gfo-like systems, yield total W masses in the range 4×10^{-5} to $2 \times 10^{-4} M_{\odot}$. Hence, broad consistency between the inferred masses from observations and theoretical predictions is found considering the involved uncertainties, which, on the theory side, include in particular the nuclear mass model employed in the nuclear network calculation. The mass determined from observation for AT2017gfo is close to the highest values predicted by our simulations, which is unsurprising due to the possibility that other lines or processes could be contributing to the feature in the observation. Concerning AT2023vfi, the comparison reveals a somewhat worse match, which may either be related to uncertainties of the inference or point to the ejection of more neutron-rich material in AT2023vfi, for which no binary mass estimates exist since no gravitational waves were recorded from this event.

Nuclear network calculations suggest that the production of W requires generally very neutron-rich conditions with an electron fraction $Y_e \leq 0.2$ (see Fig. 9). Therefore, measurements of W are useful to estimate the amount of neutron-rich material from merger observations. Exploiting tight correlations between the W abundance and the mass fraction of lanthanides and actinides, $X_{\text{La}} + X_{\text{Ac}}$, we convert the inferred mass fraction of W to an estimate of $X_{\text{La}} + X_{\text{Ac}}$. In the case of AT2017gfo, we find mass fractions of these groups of elements in the range 0.85–11 per cent of the ejecta mass. These elements featuring a very high opacity are particularly relevant for shaping the light curve of KN and estimates from the light curve suggested tentatively lower values, while observations for metal-

poor stars point to a high production in mergers if those are the dominant site of r -process nucleosynthesis. Similarly, W can be used to estimate the amount of third-peak r -process elements, which are constrained to the range 0.73–19 per cent for AT2017gfo. It is therefore possible to infer from the observational estimate of the W mass in Section 3.2 that significant amounts of third-peak r -process elements, lanthanides and actinides, will be produced along with it. Based on hydrodynamical merger models, we estimate line profiles for the W feature, which are significantly affected by the tungsten production throughout the ejecta. This indicates the possibility to probe the velocity distribution of W and possibly distinguish short-lived and long-lived merger remnants if the latter indeed generically yield a strong deficiency of W at low velocities ($v < 0.1$) as in our limited set of models. These considerations exemplify the usefulness of W to trace the properties of merger outflows and the underlying nucleosynthesis. It shows the importance of measuring W as laid out here and the need to improve observational data to more accurately determine the luminosity of features in KN spectra.

ACKNOWLEDGEMENTS

This study was funded/co-funded by the European Union (ERC, HEAVYMETAL, 101071865). Views and opinions expressed are, however, those of the author(s) only and do not necessarily reflect those of the European Union or the European Research Council. Neither the European Union nor the granting authority can be held responsible for them. OJ, GM-P, and ZX acknowledge support by the European Research Council (ERC) under the European Union’s Horizon 2020 research and innovation programme (ERC Advanced Grant KILONOVA No. 885281). AB, OJ, GM-P, and ZX acknowledge support by the Deutsche Forschungsgemeinschaft (DFG, German Research Foundation) through Project – ID 279384907 – SFB 1245 (subprojects B01, B06, and B07) and MA 4248/3-1. AB, OJ, GM-P, and ZX acknowledge funding by the State of Hesse within the Cluster Project ELEMENTS. The authors are grateful for use of the computing resources from the Northern Ireland High Performance Computing (NI-HPC) service funded by EPSRC (EP/T022175).

DATA AVAILABILITY

The atomic data used to calculate luminosities in this work will be made available on the OPEN-ADAS (2024) data base in the form of adf04 files.

REFERENCES

- Arcones A., Martínez-Pinedo G., 2011, *Phys. Rev. C*, 83, 045809
 Bahcall J. N., Wolf R. A., 1968, *ApJ*, 152, 701
 Bar-Shalom A., Klapisch M., Oreg J., 2001, *J. Quant. Spectrosc. Radiat. Transfer*, 71, 169
 Bates D. R., Kingston A., McWhirter R. P., 1962, *Proc. R. Soc. A*, 267, 297
 Bromley S. J., McCann M., Loch S. D., Ballance C. P., 2023, *ApJS*, 268, 22
 Dufflo J., Zuker A. P., 1995, *Phys. Rev. C*, 52, R23
 Dunleavy N. L., Ballance C. P., Ramsbottom C. A., Johnson C. A., Loch S. D., Ennis D. A., 2022, *J. Phys. B: At. Mol. Opt. Phys.*, 55, 175002
 Fujibayashi S., Wanajo S., Kiuchi K., Kyutoku K., Sekiguchi Y., Shibata M., 2020, *ApJ*, 901, 122
 Gillanders J. H., Smartt S. J., 2024, preprint (arXiv:2408.11093)
 Gillanders J. H., McCann M., Sim S., Smartt S., Ballance C. P., 2021, *MNRAS*, 506, 3560

- Gillanders J. H., Sim S. A., Smartt S. J., Goriely S., Bauswein A., 2024, *MNRAS*, 529, 2918
 Goriely S., 1999, *A&A*, 342, 881
 Goriely S., Chamel N., Pearson J. M., 2010, *Phys. Rev. C*, 82, 035804
 Hotokezaka K., Tanaka M., Kato D., Gaigalas G., 2022, *MNRAS*, 515, L89
 Hotokezaka K., Tanaka M., Kato D., Gaigalas G., 2023, *MNRAS*, 526, L155
 Jerkstrand A., 2017, in Alsabti A. W., Murdin P., eds, *Handbook of Supernovae*. Springer, Cham, p. 795
 Ji A. P., Drout M. R., Hansen T. T., 2019, *ApJ*, 882, 40
 Johnson C., Loch S., Ennis D., 2019, *Nucl. Mater. Energy*, 20, 100579
 Just O. et al., 2023, *ApJ*, 951, L12
 Kasliwal M. M. et al., 2019, *MNRAS*, 510, L7
 Kasliwal M. M. et al., 2022, *MNRAS*, 510, L7
 Kramida A., Ralchenko Y., Reader J., NIST ASD Team, 2024, NIST Atomic Spectra Database (version 5.11). Gaithersburg, MD, USA <https://physics.nist.gov/asd>
 Kyutoku K., Shibata M., Taniguchi K., 2021, *Living Rev. Relativ.*, 24, 5
 Levan A. J. et al., 2024, *Nature*, 626, 737
 Lippuner J., Fernández R., Roberts L. F., Foucart F., Kasen D., Metzger B. D., Ott C. D., 2017, *MNRAS*, 472, 904
 McCann M., Bromley S., Loch S. D., Ballance C. P., 2022, *MNRAS*, 509, 4723
 McCann M., Ballance C. P., Loch S., Ennis D., 2024, *J. Phys. B: At. Mol. Opt. Phys.*, 57, 235202
 Mendoza-Temis J. D. J., Wu M. R., Langanke K., Martínez-Pinedo G., Bauswein A., Janka H. T., 2015, *Phys. Rev. C*, 92, 055805
 Mulholland L. P., McElroy N. E., McNeill F. L., Sim S. A., Ballance C. P., Ramsbottom C. A., 2024a, *MNRAS*, 532, 2289
 Mulholland L. P., McNeill F., Sim S. A., Ballance C. P., Ramsbottom C. A., 2024b, *MNRAS*, 534, 3423
 OPEN-ADAS, 2024, OPEN-ADAS website. <https://open.adas.ac.uk>
 Pasternack S., 1940, *ApJ*, 92, 129
 Perego A., Rosswog S., Cabezón R. M., Korobkin O., Käppeli R., Arcones A., Liebendörfer M., 2014, *MNRAS*, 443, 3134
 Pian E. et al., 2017, *Nature*, 551, 67
 Pognan Q., Jerkstrand A., Grumer J., 2022, *MNRAS*, 510, 3806
 Roederer I. U. et al., 2022, *ApJS*, 260, 27
 Shakura N. I., Sunyaev R. A., 1973, *A&A*, 24, 337
 Shortley G. H., 1940, *Phys. Rev.*, 57, 225
 Smartt S. J. et al., 2017, *Nature*, 551, 75
 Smyth R. T., Ballance C. P., Ramsbottom C. A., Johnson C. A., Ennis D. A., Loch S. D., 2018, *Phys. Rev. A*, 97, 052705
 Sneppen A., Watson D., 2023, *A&A*, 675, A194
 Sneppen A. et al., 2024, preprint (arXiv:2411.03427)
 Summers H. P. et al., 2006, *Plasma Phys. Control. Fusion*, 48, 263
 Villar V. A. et al., 2018, *ApJ*, 862, L11
 Watson D. et al., 2019, *Nature*, 574, 497
 Wu M.-R., Barnes J., Martínez-Pinedo G., Metzger B. D., 2019, *Phys. Rev. Lett.*, 122, 062701

APPENDIX A: EFFECTIVE COLLISION STRENGTHS

The following tables contain effective collision strengths for the ions that were discussed in Section 3.1 and include the lines shown in Tables 1, 2, and 3. Tables A1, A2, and A3 contain W I, W II, and W III. Tables A4, A5, and A6 contain Pt I, Pt II, and Pt III. Tables A7, A8, and A9 contain Au I, Au II, and Au III.

Table A1. Effective collision strengths for W I.

Wavelength (nm)	Index		A-value (s ⁻¹)	Effective collision strengths				
	Lower	Upper		0.15 eV	0.25 eV	0.4 eV	0.6 eV	0.8 eV
5986.99	1	2	5.32E-02	1.03E+00	1.02E+00	1.01E+00	1.01E+00	1.00E+00
6041.42	2	4	1.27E-01	2.25E+00	2.29E+00	2.33E+00	2.37E+00	2.39E+00
6646.86	4	5	1.35E-01	3.47E+00	3.47E+00	3.47E+00	3.47E+00	3.47E+00
7197.71	5	6	9.28E-02	3.64E+00	3.70E+00	3.75E+00	3.80E+00	3.83E+00
1272.63	2	7	8.07E+00	3.42E-01	3.29E-01	3.17E-01	3.06E-01	2.99E-01
3059.94	3	6	2.33E-03	3.25E+00	3.16E+00	3.08E+00	3.01E+00	2.96E+00
1682.76	6	8	1.33E+00	1.86E+00	1.68E+00	1.51E+00	1.36E+00	1.26E+00
1001.85	4	9	5.72E+00	3.15E-01	3.08E-01	3.02E-01	2.97E-01	2.93E-01
1173.91	5	10	1.66E+00	9.83E-01	9.02E-01	8.27E-01	7.63E-01	7.17E-01
1363.89	5	8	3.45E-01	8.80E-01	7.95E-01	7.17E-01	6.50E-01	6.02E-01

Table A2. Effective collision strengths for W II.

Wavelength (nm)	Index		A-value (s ⁻¹)	Effective collision strengths				
	Lower	Upper		0.15 eV	0.25 eV	0.4 eV	0.6 eV	0.8 eV
6584.02	1	2	2.06E-01	4.07E+00	3.76E+00	3.38E+00	2.99E+00	2.74E+00
6047.25	2	3	2.80E-01	5.41E+00	5.10E+00	4.69E+00	4.25E+00	3.94E+00
6477.50	3	4	1.86E-01	7.39E+00	6.91E+00	6.33E+00	5.77E+00	5.41E+00
6989.07	4	5	8.60E-02	7.99E+00	7.61E+00	7.11E+00	6.53E+00	6.10E+00
1367.26	2	8	2.81E+00	8.95E-01	8.50E-01	7.82E-01	6.99E-01	6.44E-01
1132.15	1	8	1.26E+00	7.20E-01	6.58E-01	5.71E-01	4.82E-01	4.26E-01
1347.66	1	6	2.21E-02	7.95E-01	7.72E-01	7.18E-01	6.49E-01	6.04E-01
1347.71	3	9	7.06E-01	1.96E+00	1.84E+00	1.65E+00	1.45E+00	1.31E+00
1694.50	2	6	1.93E-02	2.01E+00	1.95E+00	1.84E+00	1.69E+00	1.60E+00
1805.45	3	7	2.74E-02	1.88E+00	1.86E+00	1.75E+00	1.57E+00	1.44E+00

Table A3. Effective collision strengths for W III.

Wavelength (nm)	Index		A-value (s ⁻¹)	Effective collision strengths				
	Lower	Upper		0.15 eV	0.25 eV	0.4 eV	0.6 eV	0.8 eV
4432.23	1	2	5.04E-01	1.74E+00	1.58E+00	1.43E+00	1.30E+00	1.21E+00
4535.16	2	3	5.40E-01	4.59E+00	4.11E+00	3.67E+00	3.29E+00	3.02E+00
5504.75	3	4	2.60E-01	5.79E+00	5.28E+00	4.81E+00	4.41E+00	4.12E+00
1307.51	2	6	6.98E+00	6.23E-01	5.50E-01	4.83E-01	4.25E-01	3.84E-01
7097.87	4	5	7.13E-02	8.00E+00	7.21E+00	6.48E+00	5.84E+00	5.40E+00
1536.73	3	7	1.35E-01	1.81E+00	1.63E+00	1.47E+00	1.33E+00	1.23E+00
1187.67	3	9	3.60E+00	1.38E+00	1.24E+00	1.11E+00	9.98E-01	9.18E-01
804.69	1	8	9.31E-02	9.05E-01	8.10E-01	7.23E-01	6.47E-01	5.94E-01
1662.71	5	10	6.07E-01	4.79E+00	4.26E+00	3.77E+00	3.35E+00	3.05E+00
1147.80	2	7	3.00E-02	1.51E+00	1.36E+00	1.22E+00	1.10E+00	1.02E+00

Table A4. Effective collision strengths for Pt I.

Wavelength (nm)	Index		A-value (s ⁻¹)	Effective collision strengths				
	Lower	Upper		0.15 eV	0.25 eV	0.4 eV	0.6 eV	0.8 eV
1522.66	1	5	5.25E-01	2.69E+00	2.51E+00	2.34E+00	2.19E+00	2.09E+00
12 888.66	1	2	4.09E-04	5.16E+00	4.88E+00	4.61E+00	4.38E+00	4.22E+00
1076.07	3	6	2.52E+00	9.62E-01	9.14E-01	8.70E-01	8.32E-01	8.05E-01
1726.65	2	5	1.40E-02	2.35E+00	2.19E+00	2.05E+00	1.93E+00	1.84E+00
1068.83	2	7	1.16E+00	8.73E-01	7.77E-01	6.89E-01	6.13E-01	5.59E-01
1864.18	2	4	4.36E-04	8.20E-01	7.40E-01	6.66E-01	6.02E-01	5.57E-01
740.95	1	8	9.59E-01	1.91E+00	1.80E+00	1.69E+00	1.59E+00	1.53E+00
1070.57	2	6	1.22E-01	1.30E+00	1.26E+00	1.22E+00	1.18E+00	1.16E+00
2805.51	5	7	1.32E-01	1.50E+00	1.41E+00	1.33E+00	1.26E+00	1.21E+00
1741.01	3	5	7.74E-05	2.02E+00	1.81E+00	1.61E+00	1.44E+00	1.32E+00

Table A5. Effective collision strengths for Pt II.

Wavelength (nm)	Index		A-value (s ⁻¹)	Effective collision strengths				
	Lower	Upper		0.15 eV	0.25 eV	0.4 eV	0.6 eV	0.8 eV
2188.35	2	4	2.54E+00	1.35E+01	1.24E+01	1.14E+01	1.05E+01	9.84E+00
1187.67	1	3	9.05E+00	1.82E+00	1.71E+00	1.61E+00	1.52E+00	1.46E+00
1068.80	1	4	1.10E-01	2.39E+00	2.28E+00	2.17E+00	2.07E+00	2.01E+00
2517.02	4	5	1.96E+00	4.49E+00	4.11E+00	3.76E+00	3.47E+00	3.25E+00
633.26	1	6	3.85E+00	1.41E+00	1.33E+00	1.25E+00	1.19E+00	1.14E+00
2036.89	3	5	2.68E-01	2.02E+00	1.86E+00	1.71E+00	1.58E+00	1.49E+00
2089.14	1	2	6.17E-06	3.07E+00	2.96E+00	2.86E+00	2.77E+00	2.71E+00
1339.65	4	7	6.46E+00	2.88E+00	2.65E+00	2.44E+00	2.26E+00	2.13E+00
751.25	2	8	1.52E+01	3.83E+00	3.46E+00	3.13E+00	2.85E+00	2.64E+00
750.23	1	5	3.93E-02	2.16E+00	2.05E+00	1.95E+00	1.86E+00	1.80E+00

Table A6. Effective collision strengths for Pt III.

Wavelength (nm)	Index		A-value (s ⁻¹)	Effective collision strengths				
	Lower	Upper		0.15 eV	0.25 eV	0.4 eV	0.6 eV	0.8 eV
1025.46	1	3	4.66E+01	4.27E+00	4.11E+00	3.97E+00	3.85E+00	3.76E+00
1126.28	2	4	2.22E+01	2.83E+00	2.60E+00	2.39E+00	2.21E+00	2.08E+00
2242.86	2	3	1.13E+00	3.82E+00	3.56E+00	3.33E+00	3.12E+00	2.98E+00
870.44	2	6	2.10E+01	1.61E+00	1.47E+00	1.34E+00	1.23E+00	1.15E+00
2262.34	3	4	3.05E+00	3.73E+00	3.43E+00	3.16E+00	2.93E+00	2.76E+00
468.81	1	7	1.91E+01	2.68E+00	2.65E+00	2.62E+00	2.60E+00	2.58E+00
3831.85	4	6	4.05E-01	2.12E+00	1.99E+00	1.88E+00	1.78E+00	1.71E+00
863.63	3	7	1.94E+00	4.02E+00	3.68E+00	3.38E+00	3.12E+00	2.93E+00
457.94	1	8	1.02E-02	3.11E+00	3.07E+00	3.04E+00	3.01E+00	2.99E+00
5427.12	5	6	2.00E-01	5.85E-01	5.37E-01	4.92E-01	4.53E-01	4.26E-01

Table A7. Effective collision strengths for Au I.

Wavelength (nm)	Index		A-value (s ⁻¹)	Effective collision strengths				
	Lower	Upper		0.15 eV	0.25 eV	0.4 eV	0.6 eV	0.8 eV
1091.56	1	2	2.48E-02	1.55E+00	1.49E+00	1.45E+00	1.41E+00	1.38E+00
814.73	2	3	2.98E+01	6.45E-01	6.06E-01	5.70E-01	5.39E-01	5.17E-01
466.52	1	3	1.31E+00	1.10E+00	1.02E+00	9.48E-01	8.87E-01	8.44E-01
267.67	1	4	1.61E+08	8.30E-01	9.85E-01	1.13E+00	1.25E+00	1.34E+00
242.87	1	5	2.26E+08	9.96E-01	1.28E+00	1.55E+00	1.78E+00	1.94E+00
303.01	2	6	1.37E+05	2.34E+00	2.33E+00	2.31E+00	2.30E+00	2.29E+00
627.99	3	4	2.33E+06	4.18E-02	1.32E-01	2.16E-01	2.88E-01	3.39E-01
312.37	2	5	2.60E+07	2.60E-01	3.50E-01	4.34E-01	5.06E-01	5.57E-01
274.91	2	7	1.43E+06	4.47E+00	4.10E+00	3.76E+00	3.47E+00	3.26E+00
268.69	2	9	1.21E+06	2.10E+00	2.11E+00	2.13E+00	2.14E+00	2.15E+00

Table A8. Effective collision strengths for Au II.

Wavelength (nm)	Index		A-value (s ⁻¹)	Effective collision strengths				
	Lower	Upper		0.15 eV	0.25 eV	0.4 eV	0.6 eV	0.8 eV
566.87	1	3	4.05E-01	5.29E-01	5.76E-01	6.18E-01	6.55E-01	6.81E-01
3844.62	2	3	2.87E-01	7.68E+00	7.61E+00	7.54E+00	7.48E+00	7.44E+00
987.64	3	4	2.72E+01	2.00E+00	1.78E+00	1.57E+00	1.40E+00	1.27E+00
685.79	2	5	2.71E+01	1.74E+00	1.60E+00	1.47E+00	1.36E+00	1.28E+00
337.60	1	5	8.27E+00	9.88E-01	9.16E-01	8.50E-01	7.92E-01	7.52E-01
834.68	3	5	1.74E+00	1.60E+00	1.50E+00	1.41E+00	1.34E+00	1.28E+00
785.78	2	4	4.98E-03	7.74E-01	6.96E-01	6.24E-01	5.62E-01	5.18E-01
5389.40	4	5	5.42E-02	5.07E+00	4.94E+00	4.83E+00	4.73E+00	4.66E+00
393.09	2	6	5.34E+00	2.09E+00	2.61E+00	3.09E+00	3.51E+00	3.80E+00
437.86	3	6	7.39E-01	1.61E+00	1.74E+00	1.85E+00	1.95E+00	2.02E+00

Table A9. Effective collision strengths for Au III.

Wavelength (nm)	Index		A-value (s ⁻¹)	Effective collision strengths				
	Lower	Upper		0.15 eV	0.25 eV	0.4 eV	0.6 eV	0.8 eV
787.77	1	2	3.30E+01	3.39E+00	3.36E+00	3.33E+00	3.31E+00	3.29E+00
336.09	1	3	1.34E-01	2.66E+00	2.56E+00	2.47E+00	2.38E+00	2.33E+00
285.09	1	4	1.05E+01	2.39E+00	2.29E+00	2.20E+00	2.11E+00	2.06E+00
1878.69	3	4	3.72E+00	1.17E+01	1.10E+01	1.03E+01	9.73E+00	9.32E+00
257.58	1	5	7.95E+00	1.69E+00	1.59E+00	1.50E+00	1.43E+00	1.37E+00
247.86	1	6	2.04E+01	9.73E-01	9.49E-01	9.27E-01	9.07E-01	8.94E-01
382.73	2	5	1.09E+00	1.56E+00	1.37E+00	1.20E+00	1.05E+00	9.43E-01
446.77	2	4	2.78E-02	1.27E+00	1.17E+00	1.08E+00	1.01E+00	9.52E-01
2669.87	4	5	1.01E+00	5.10E+00	4.90E+00	4.73E+00	4.58E+00	4.47E+00
225.09	1	7	1.72E+01	1.11E+00	1.10E+00	1.08E+00	1.07E+00	1.06E+00

This paper has been typeset from a $\text{\TeX}/\text{\LaTeX}$ file prepared by the author.